Computational and Structural Biotechnology Journal 23 (2024) 4047–4063

Contents lists available at ScienceDirect

Computational and Structural Biotechnology Journal

journal homepage: www.elsevier.com/locate/csbj

Research article

Conformational plasticity links structural instability of NAA10^{F128I} and NAA10^{F128L} mutants to their catalytic deregulation

Smita Saha [a,b,1], Buddhi Prakash Jain [c,2], Debasish Kumar Ghosh [d,*,3], Akash Ranjan [a,*,4]

[a] Computational and Functional Genomics Group, BRIC-Centre for DNA Fingerprinting and Diagnostics, Hyderabad, Telangana, India
[b] Graduate Studies, Manipal Academy of Higher Education, Manipal, Karnataka, India
[c] Department of Zoology, Mahatma Gandhi Central University, Motihari, Bihar, India
[d] Kasturba Medical College, Manipal Academy of Higher Education, Manipal, Karnataka, India

ARTICLE INFO

Keywords:
Catalysis
N-terminal acetylation
N-α-acetyltransferase 10
Mutation
Structural instability, Loss of enzymatic function

ABSTRACT

The acetylation of proteins' N-terminal amino groups by the N-acetyltransferase complexes plays a crucial role in modulating the spatial stability and functional activities of diverse human proteins. Mutations disrupting the stability and function of NAA10 result in X-linked rare genetic disorders. In this study, we conducted a global analysis of the impact of fifteen disease-associated missense mutations in *NAA10*. The analyses revealed that mutations in specific residues, such as Y43, V107, V111, and F128, predictably disrupted interactions essential for NAA10 stability, while most mutations (except R79C, A111W, Q129P, and N178K) expectedly led to structural destabilization. Mutations in many conserved residues within short linear motifs and post-translational modification sites were predicted to affect NAA10 functionality and regulation. All mutations were classified as pathogenic, with F128I and F128L identified as the most destabilizing mutations. The findings show that the F128L and F128I mutations employ different mechanisms for the loss of catalytic activities of NAA10^{F128L} and NAA10^{F128I} due to their structural instability. These two mutations induce distinct folding energy states that differentially modulate the structures of different regions of NAA10^{F128L} and NAA10^{F128I}. Specifically, the predicted instability caused by the F128I mutation results in decreased flexibility within the substrate-binding region, impairing the substrate peptide binding ability of NAA10^{F128I}. Conversely, F128L is predicted to reduce the flexibility of the region containing the acetyl-CoA binding residues in NAA10^{F128L}. Our study provides insights into the mechanism of catalytic inactivation of mutants of NAA10, particularly elucidating the mechanistic features of the structural and functional pathogenicity of the F128L and F128I mutations.

1. Introduction

Cellular proteostasis depends on post-translational modifiers' catalytic activities, regulating protein stability and function [1]. Post-translational modifications (PTMs) like acetylation, phosphorylation, and ubiquitination maintain protein folding, function, and degradation equilibrium [2, 3]. N-terminal acetylation (NTA) is a co-translational or post-translational modification catalyzed by N-acetyl transferase complexes, involving the addition of an acetyl group to the α-amino group of a protein's N-terminal residue [4]. NTA plays a crucial role in cellular proteostasis by regulating protein stability, folding, localization, and interactions [5]. It influences the electrostatic properties and hydrophobicity of nascent polypeptides, impacting their interactions with chaperones during folding [6]. Additionally, NTA serves as a sorting signal for directing proteins to specific cellular compartments, ensuring their proper functionality [7]. It also modulates protein-protein interactions, affecting macromolecular complex formation and signaling cascades [8]. Notably, NTA regulates protein half-life by either protecting proteins from degradation or targeting them for degradation by specific proteases or the proteasome, thus influencing

* Corresponding authors.
E-mail addresses: smitasaha2920@gmail.com (S. Saha), buddhiprakash@mgcub.ac.in (B.P. Jain), dghosh7@gmail.com (D.K. Ghosh), akash@cdfd.org.in (A. Ranjan).
[1] 0000-0002-5534-1131
[2] 0000-0002-7225-7257
[3] 0000-0002-9196-0685
[4] 0000-0002-4582-1553

https://doi.org/10.1016/j.csbj.2024.11.014
Received 29 September 2024; Received in revised form 5 November 2024; Accepted 5 November 2024
Available online 8 November 2024

protein turnover [9–12].

The N-terminal acetyltransferase complex A (NatA) comprises catalytic subunit NAA10 (ARD1) and auxiliary subunit NAA15 (NARG1) in a stable heterodimer [13–15]. NAA10 acetylates exposed N-terminal residues [15], while NAA15 aids substrate specificity and complex stability [15]. NatA recognizes substrates through a specific motif and binds to acetyl-CoA, transferring the acetyl group to the substrate's N-terminal residue [16]. The catalytic cycle follows a ping-pong mechanism involving a covalent intermediate formation before acetyl group transfer [17]. Specific amino acid residues, including conserved lysine, aid in coordinating acetyl-CoA and substrate binding [18]. Removal of the initiator methionine by methionine aminopeptidases precedes NatA-mediated NTA of proteins with serine, alanine, threonine, valine, glycine, and cysteine in second position [19].

NAA10, a small protein, contains regions for NAA15 interaction, N-acetyltransferase activity, and a charge-rich low complexity region [15, 20]. Its functions span cellular processes like proliferation, migration, and differentiation [21], regulating various proteins including UPK1B, beta-catenin, and ADAM9 [22–24]. It maintains osteoblast differentiation through RUNX regulation [25] and suppresses cell migration by acetylating STAT5A and RAC1 [26, 27] while interfering with the PIRH2-P53 signaling pathway [28]. NAA10's acetylation of HSP70 and HIF1A is involved in protein folding and degradation, respectively [29, 30]. It causes the disassociation of AR from the HSP90 complex [31], and facilitates regulating gene transcription such as PXR [32, 33]. NAA10 undergoes various post-translational modifications, including phosphorylation and self-acetylation [34, 35]. These post-translational modifications are speculated to regulate the activity, interactions, and stability of NAA10 [34, 35].

Deregulated *NAA10* mutations, primarily missense, are linked to X-linked rare genetic disorders known as *NAA10*-related neurodevelopmental syndromes [36–46]. These include Ogden syndrome (OGDNS; MIM #300855) and syndromic microphthalmia 1 (MCOPS1; MIM #309800). Ogden syndrome usually presents in infancy with severe developmental delays, intellectual disability, failure to thrive, weak muscle tone, and distinctive facial features, often leading to premature death due to cardiac arrest or respiratory failure in males [36–46]. Various Ogden disease-associated NAA10 protein mutations, such as A6P, H16P, S37P, Y43S, R79C, R83C, L86R, V107F, V111G, A117W, F128L, Q129P, R149W, E157K, and N178K, are linked to a range of clinical features, including severe postnatal growth failure, global developmental delays, various congenital abnormalities such as cardiac defects and distinctive dysmorphic facial features, such as a wrinkled forehead, prominent eyes, and microretrognathia. Each NAA10 mutation introduces specific changes in amino acids that can predictably disrupt the protein's structure and stability. For instance, A6P and H16P replace flexible residues with proline, putatively introducing rigidity that distorts local structures, while S37P and Q129P alter key functional sites by substituting polar residues with proline, leading to potential loss of flexibility and stability. Mutations like R79C and R83C disrupt critical electrostatic interactions due to the substitution of charged arginine with cysteine. Similarly, L86R and R149W introduce charged residues in hydrophobic regions, likely destabilizing the protein's hydrophobic core. Other mutations, such as V107F and A117W, introduce bulkier residues, which may cause steric hindrance and alter hydrophobic packing, further affecting stability and function. The E157K and N178K mutations involve charge reversals that predictably disrupt salt bridges, critically impacting the protein's structural integrity. Overall, these mutations highlight the delicate balance of interactions within NAA10, where alterations can lead to significant functional consequences and contribute to the associated clinical phenotypes. In general, mutations in NAA10 disrupt global proteome N-terminal acetylation, causing widespread cellular dysfunction, particularly affecting the heart and brain, contributing to severe symptoms and often fatal outcomes. Genotype-phenotype correlation indicates overlapping features among NAA10-related syndromes [36–46].

The pathogenic mutations F128L and F128I impair the cellular stability and functional activity of NAA10 [43–45]. The F128L (due to c .384 T > G) mutation was observed in a sixteen-year-old with severe neurodevelopmental disorder [43]. F128L mutation due to c .384 T > A change in *NAA10* mRNA was also observed in another proband [44]. The F128I was reported in an individual with intellectual disability and developmental delay [44]. *In vitro* assays demonstrated reduced catalytic activity and stability of $NAA10^{F128L}$ and $NAA10^{F128I}$ compared to wild-type NAA10 [43]. A recent study [44] indicates that the mutations F128L and F128I in NAA10 lead to both structural destabilization and a significant loss of catalytic function. These mutations might interfere with the overall structure of NAA10, causing reduced protein stability and loss of NAA10's NAT activity. Another recently reported F128S mutation in the NAA10 is likely to destabilize the protein's structure and catalytic function by disrupting hydrophobic core interactions [39]. Despite genotype-to-phenotype characterization, the mechanism behind instability and loss of function due to these mutations remains unclear.

This study explored the impact of fifteen disease-associated mutations in NAA10 on stability, catalytic function, and interactions. Through conservation analysis and structure prediction, it was found that F128 is critical for NAA10 stability and function. Mutations F128I and F128L are predicted to induce global and local conformational changes. F128I affects substrate peptide binding groove flexibility, while F128L disrupts acetyl-CoA binding interactions, resulting in decreased catalytic activity. Despite occurring at the same position, these mutations lead to enzyme activity reduction via distinct mechanisms. Moreover, differences in folding patterns between wild-type and mutant NAA10 proteins highlight the detrimental effects of these mutations on protein structure and stability.

2. Results

2.1. Assessment of the disease-associated missense mutations of NAA10

In the beginning of the study, we aimed to investigate the impact of various disease-associated missense mutations of NAA10. We curated fifteen missense mutations of NAA10 reported in various studies of Ogden disease and microphthalmia syndromic 1 (Fig. 1A), and globally analyzed the effects of the mutations on different aspects of NAA10 as described below-

(a) Structure: to show the effects of mutations on NAA10 structure, we analyzed the protein structure network (PSN), a representative network that shows covalent and non-covalent interactions between residues in a protein. The hub residues in the PSN are of great importance because they can form a larger number of interactions with other residues. Mutation of a hub can affect the integrity of the network and the structural stability of the protein. We constructed the PSN of NAA10 based on the cumulative number of hydrogen bonds, hydrophobic interactions, salt bridges, and van der Waals interactions displayed by the side chains of the residues (Fig. 1B). We defined an amino acid as a hub if the total number of interactions displayed by the residues is ≥ 5. In the contact-based PSN of NAA10, Y43, V107, V111, and F128 are the hubs (Fig. 1B). Since most of these residues are hydrophobic, a significant number of their interactions are hydrophobic in nature. Substitution of these residues by other amino acids, as observed in Ogden disease, would disrupt the conserved interactions and ultimately affect the structural stability of NAA10. For example, in wild-type NAA10, F128 showed base stacking interactions with Y122 in addition to forming hydrogen bonds and hydrophobic interactions with the M91, V107, L109, K148, and R149 residues (Fig. 1B). In contrast, the interactions of L128 of $NAA10^{F128L}$ were limited to M147 and R149.

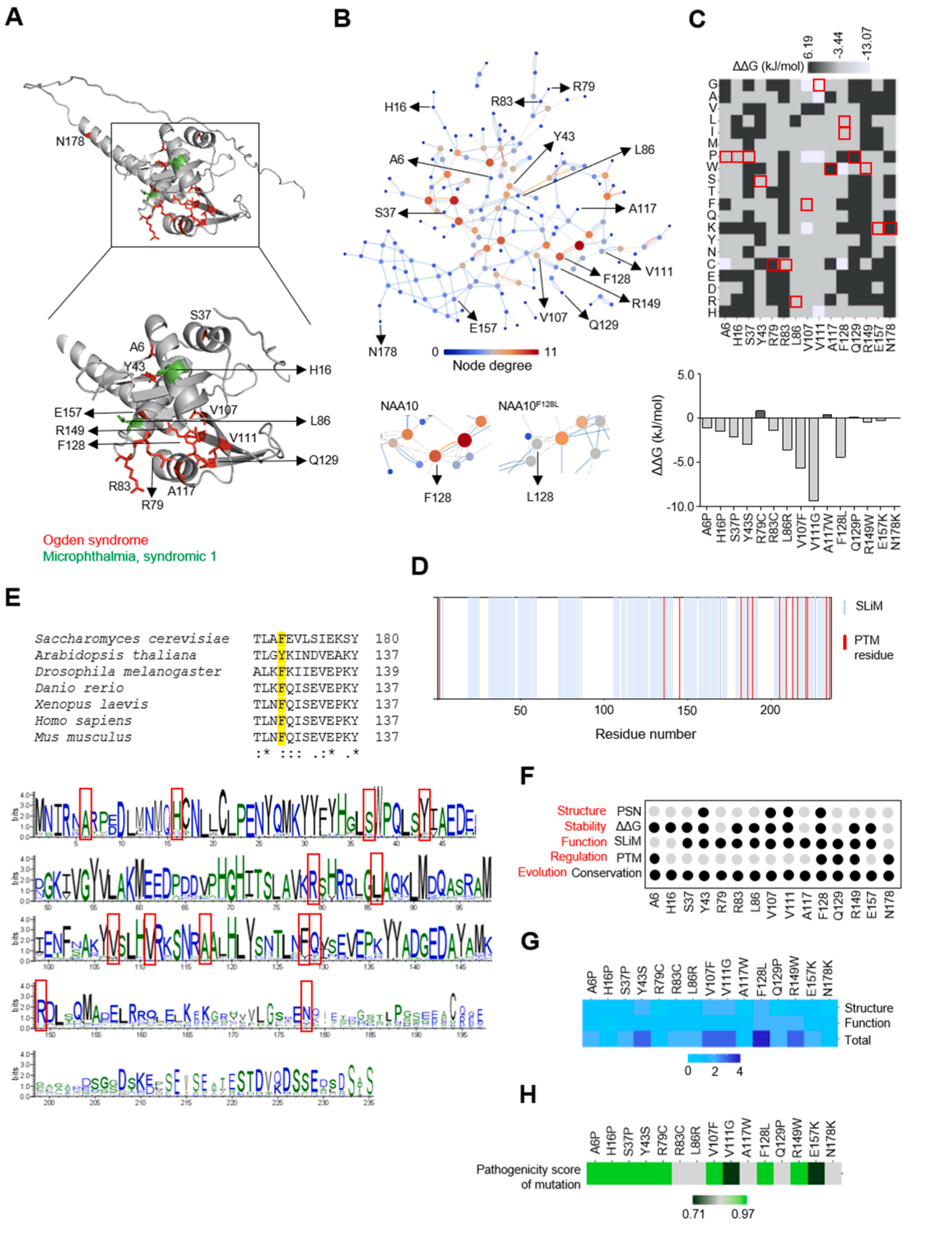

(caption on next page)

Fig. 1. Analysis of the destabilization and pathogenic potential of the various mutations in the global perspective of different NAA10 mutations involved in different genetic diseases. (A) Representation of the different residues mutated in the NAA10 protein. The color scheme of the mutations corresponds to the names of the mentioned diseases. (B - E) Integrated classification of NAA10 residues showing reported mutations in different genetic diseases. The descriptors are: the protein structure network (PSN) representing the structural significance of each mutated residue, the free energy change of protein folding due to mutation (ΔΔG) accounting for mutation-induced stability changes [analyzed in FoldX], short linear interacting motifs (SLiMs), overlapping mutation sites that predict the functional significance of the mutated residue, posttranslational modifications (PTMs) of the mutation-inducing regions that denote regulation, and sequence conservation that describes the evolutionary selectivity of the residues. (F) Mutations that alter or affect the above properties are highlighted as black circles linking each mutation to a specific effect. (G) Heat map based on the collective scores of structure and function in relation to the damage potential of mutations as described in 1B-1F. A higher score indicates a higher damage potential from the mutation. (H) PolyPhen-2 score describes the pathogenicity potential of missense mutations of NAA10. Higher Polyphen-2 scores in 0–1 scale describe higher pathogenicity potential of variants, whereas a Polyphen-2 score of a variant above 0.5 indicates that the variant is pathogenic.

(b) Stability: to understand how mutation of a residue in NAA10 might perturb the overall structural stability of the protein, we estimated the changes in folding free energy for each mutation of NAA10 associated with diseases (Fig. 1C). Interestingly, all mutations except R79C, A117W, Q129P, and N178K showed structural destabilization, suggesting that the affected residues in wild-type NAA10 cannot accept substitutions.

(c) Function and regulation: the effects of mutations on the regulation and functionality of NAA10 were assessed by examining whether a mutation was in a short linear motif (SLiM) and whether the mutation was likely to cause changes in the post-translational modification (PTM) of NAA10. A NAA10 mutation could be functionally destabilizing if it is in a SLiM, whereas the mutation could be deregulatory if it alters the PTM of the mutated residue and one or more of its neighboring residues. Many of the NAA10 mutations were destabilizing based on their SLiM and PTM properties (Fig. 1D). For example, F128 is located in a SLiM (residues 111-134) that putatively binds to STAP1 and CK2 (the probability values of CK2 and STAP1 binding to residues 111-134 of NAA10 were $1.457e^{-02}$ and $1.026e^{-03}$, respectively). The putative kinase function of CK2 requires a negative charge at + 3 positions after the modification residue, and S131 of the ^{128}FQISEVE^{134} stretch of NAA10 is a putative site to undergo CK2-mediated phosphorylation. Indeed, the phosphorylation of S131 of NAA10 is reported in a study [47]. Therefore, CK2 could be speculated to bind the SLiM region near S131. Similarly, the scaffolding function of STAP1 (an adaptor protein with an SH2 and a PH class lipid-binding domain) recognizes a consensus sequence [(Y)(DESTA)xx(ILVFMWYA)] of the interacting protein. The ^{122}YSNTL^{126} stretch of NAA10 could putatively function as a SLiM for STAP1 binding. Therefore, the F128L and F128I mutations are expected to not only affect the binding of STAP1 and CK2 to NAA10, but this mutation may also alter the phosphorylation status of the NAA10 (Fig. 1D).

(d) Evolution: a conservation analysis describes the evolution of one or more amino acids at specific sites in NAA10. A robust occurrence of an amino acid at a particular site would indicate its irreplaceability. All of the NAA10 mutations, including F128L and F128I, occur at the conserved sites (Fig. 1E). Therefore, the mutations in the conserved residues would likely generate unfavorable consequences on the structural and functional landscape of NAA10. Multiple sequence alignment of NAA10 proteins of different organisms show that the 128th position of NAA10 prefers aromatic amino acids (Fig. 1E). Substitution of this aromatic amino acid with a small aliphatic amino acid, such as leucine and isoleucine in NAA10^{F128L} and NAA10^{F128I}, would, as expected, affect the local stability of the region near the substitution. In fact, the L128 of NAA10^{F128L} shows lower interaction energies with the neighboring residues compared to the interaction energies of F128 (of NAA10) with the neighboring residues, indicating the structural importance of an aromatic amino acid at position 128 of NAA10.

Integration of these results mapped only one mutation – F128L of NAA10 – as most strongly destabilizing the structure-function association (Fig. 1F). An additional ranking of mutations grouped all mutations into classes of high to mild damage. While F128L mutation predictably alters both stability and functionality of NAA10, some mutations are predicted not to affect stability (R79C, A117W, Q129P, and N178K), and a single mutation (H16P) does not alter functionality without affecting stability (Figs. 1F, 1G). Notably, all other mutations could be intermediately ranked to partially affect both the stability and functionality of NAA10 (Figs. 1F, 1G).

We also annotated the pathogenic potential of all the mutations using the pathogenicity scores obtained from the sequence analysis in Polymorphism Phenotyping version-2 (PolyPhen-2), CADD and REVEL. All mutations were analyzed as pathogenic variants (Fig. 1H, supporting table ST1).

2.2. *F128L and F128I mutations change the principal motion and folding dynamics of the NAA10^{F128L} and NAA10^{F128I}*

In dynamic conditions, protein acquires different functional states through global conformational transitions by collective displacement of protein backbone atoms. To investigate the concerted dynamics and functional displacements of protein backbone atoms, we conducted unrestrained molecular dynamics simulations of NAA10, NAA10^{F128L}, and NAA10^{F128I}. Based on the MSD results, we constructed and analyzed dynamic cross-correlation matrices (DCCM) for wild-type NAA10, NAA10^{F128I}, and NAA10^{F128L} (Fig. 2A). The DCCM analyses showed an increase in correlated motions of NAA10, NAA10^{F128L}, and NAA10^{F128I}, implying changes in the intra-molecular interactions due to the F128L and F128I mutations (Fig. 2A). Interestingly, the intra-molecular positive correlation in mutants did not change significantly. This was represented by a broadly similar pattern of positively correlated motions in the wild-type and mutants of NAA10 (Fig. 2A). However, the relative values were enhanced into a strong positive correlation in NAA10^{F128L} and NAA10^{F128I}. Additionally, several newly formed negative correlations were observed in NAA10^{F128L} and NAA10^{F128I} (Fig. 2A). In NAA10^{F128I}, a newly formed negative correlation between the N-terminal loop α1-α2 and the C-terminal loop β6-β7 was observed, indicating that F128I mutation disrupted the interactions between the residues which formed the substrate peptide binding pocket in NAA10. This observation supported the notion that F128I mutation may impair the flexibility of the substrate peptide binding region.

In addition to the DCCM, principal component analysis (PCA) was done by reducing the complexity of collective motions (Fig. 2B). The overall combined motion of the Cα atoms of protein structures was described by principal components 1 and 2 (PC1 and PC2). The PC1 projected the direction of most variations and PC2 projected the direction of the second most variations. On these projections, the conformational distribution of the mutant proteins covered the broader phase space compared to wild-type protein- 7.1 nm^2, 9.6 nm^2, and 12 nm^2 for wild-type NAA10, NAA10^{F128I}, and NAA10^{F128L} respectively (Fig. 2B). Phase space is a multi-dimensional space representing all possible states of a system, with each point corresponding to a specific configuration of the protein. Because of the larger area of phase space, the diversity of conformations that the mutant proteins could explore were greater,

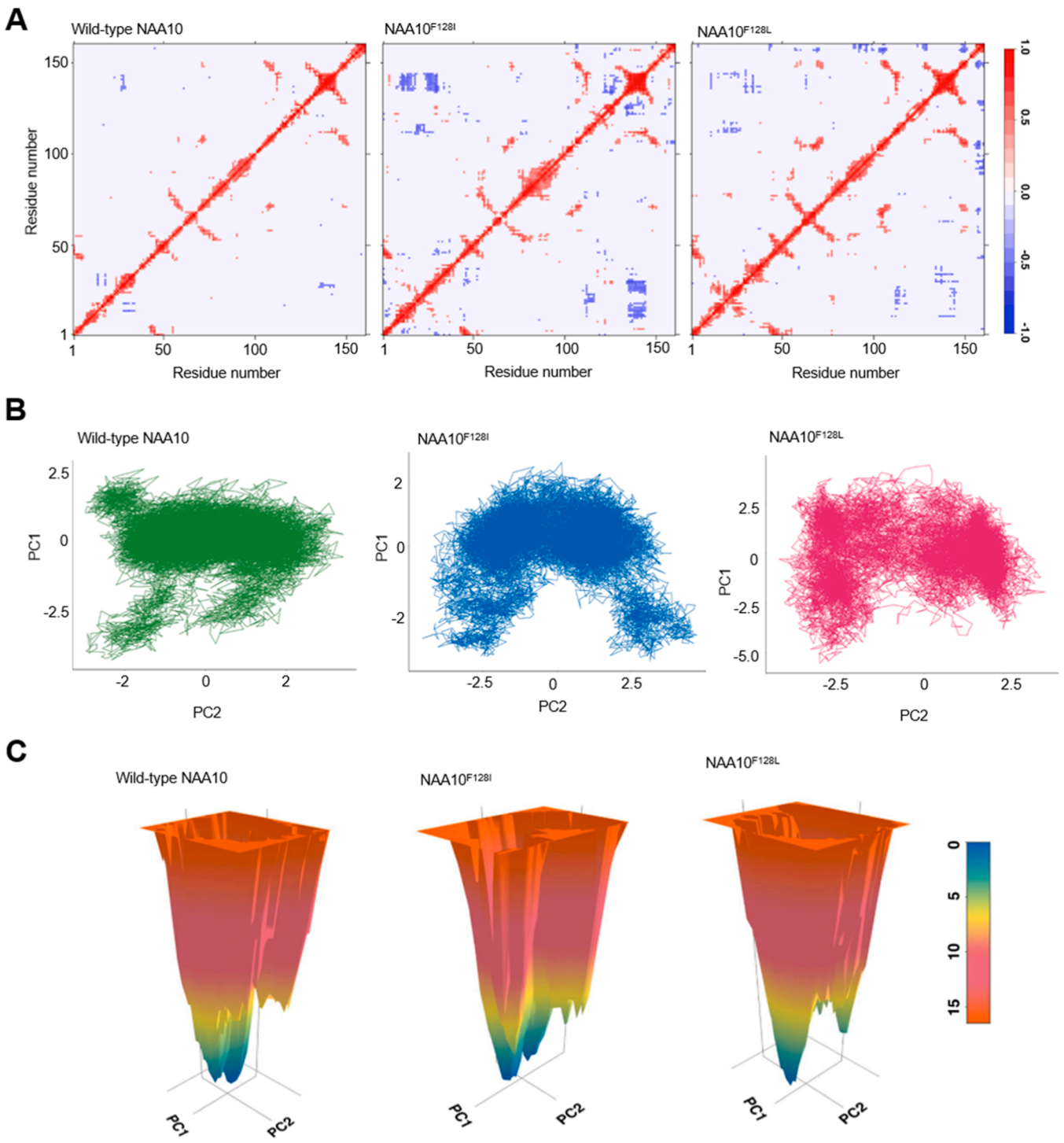

Fig. 2. F128I and F128L mutations change the principal motion and folding dynamics of NAA10^{F128I} and NAA10^{F128L} proteins. (A) The dynamical cross-correlation map (DCCM) of essential dynamics analysis reveals enhanced intra-molecular and several newly formed anti-correlations upon F128I and F128L mutations. (B) Principal component analyses show mutant systems covered the broader phase space along with two dominant principal components. (C) Gibb's free energy landscape plots show more energy states separated by low and high energy barriers in NAA10^{F128I} and NAA10^{F128L} mutants compared to wild-type NAA10.

suggesting that the mutant proteins might experience more extensive movements and variations in structure. Therefore, the NAA10^{F128L} and NAA10^{F128I} were capable of adopting a wider variety of conformations compared to the wild-type NAA10. In proteins, correlated motions indicate functional interactions between different domains or regions of the protein. For the mutants, higher eigenvalues suggested that these correlated motions were amplified, leading to greater fluctuations in their structures. As such, conformations of NAA10^{F128L} and NAA10^{F128I} were less stable and more prone to significant changes. Overall, the findings suggest that the mutations in NAA10 (F128I and F128L) lead to a protein structure that is more dynamic and less stable than the wild-type NAA10.

Next, the free energy landscape (FEL) analysis was carried out to understand a proteins' folding patterns and conformational dynamics. The FEL for wild-type and mutant proteins were constructed from the first two principal components to find any alteration in the protein

folding pattern by the F128L and F128I mutations. The FEL showed that the wild-type protein remained in one energy state (Fig. 2C). In contrast, NAA10^{F128L} and NAA10^{F128I} showed more than one energy state separated by low (in NAA10^{F128I}) and high-energy barriers (in NAA10^{F128L}) (Fig. 2C). Such FEL patterns show the diverse folding state of mutants of NAA10 (Fig. 2C).

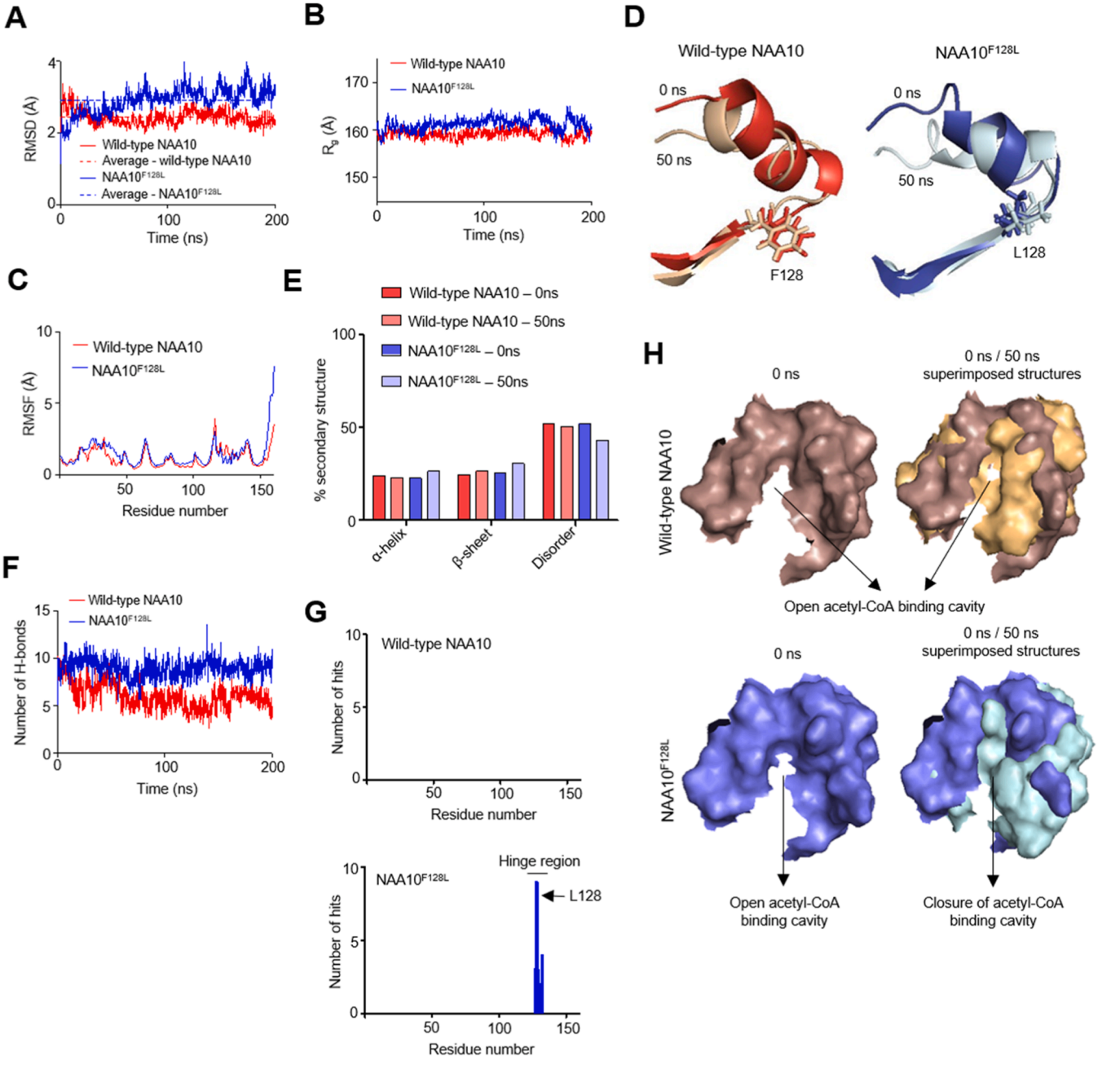

Fig. 3. Retention of the helical structure near the L128 leads to rigidity-coupled instability of the acetyl-CoA binding cavity and its residues in NAA10^{F128L}. (A) Higher RMSD values of the backbone of NAA10^{F128L} compared to RMSD values of the backbone of wild-type NAA10 indicate instability of NAA10^{F128L} during the course of molecular dynamics simulation. (B) The radius of gyration [R_g] of NAA10^{F128L} and NAA10, showing more relaxed and expanded globular structure of NAA10^{F128L} over simulation time. (C) RMSF values of the residues of NAA10^{F128L} and NAA10. Lower RMSF values of L128-neighboring residues of NAA10^{F128L} show relative instability of these residues compared to F128-neighboring residues of wild-type NAA10. (D) Structure of the F128-neighbouring and L128-neighbouring residues of NAA10 and NAA10^{F128L} at 0 ns and 50 ns of simulation. F128-neighbouring residues of NAA10 show loss of helical structures, whereas L128-neighbouring residues of NAA10^{F128L} retained the helical structure over simulation time. (E) Analysis of the secondary structure composition of NAA10 and NAA10^{F128L} at 0 ns and 50 ns of simulation shows an increase of helical structure and loss of disordered region in NAA10^{F128L} over the simulation time. (F) The number of hydrogen bonds of the residues of α5, loop α5-β6, and β6 of NAA10 and NAA10^{F128L}. The number of intra-molecular hydrogen bonds is increased in the α5, loop α5-β6, and β6 of NAA10^{F128L} compared to the wild-type NAA10. (G) The L128 and its nearby amino acids are hinge-forming residues in NAA10^{F128L}, whereas no residue in NAA10 acts to form hinges. (H) Structural representation of acetyl-CoA binding cavity of NAA10 and NAA10^{F128L} at 0 ns and 50 ns of simulation. The opening of the acetyl-CoA binding cavity of NAA10 remains open over the simulation time, whereas the opening of the acetyl-CoA binding cavity is gradually closed in NAA10^{F128L} due to structural transitions of the region.

2.3. F128L mutation causes destabilizing conformational rigidity to acetyl-CoA binding residues of NAA10^{F128L}

Missense mutations are known to induce structural changes in proteins. Such mutations modulate the local or global conformational changes in protein structure, leading to loss of stability, localization, and functions of respective proteins.

The missense mutations at position F128 of NAA10 are identified as potentially damaging due to the putative loss of structure-function stability in mutants such as NAA10^{F128L} and NAA10^{F128I}. In order to understand how the F128L variation in NAA10 led to the mutant protein's dysfunction, we performed unrestrained molecular dynamics simulations (MDS) of the wild-type NAA10 and NAA10^{F128L}. MDS results show that the overall conformation and stability of NAA10^{F128L} deviate from the conformational and stability dynamics of NAA10. Although it was noted that the root mean square deviation (RMSD) values of the backbone of both NAA10^{F128L} and NAA10 attained considerable stabilities over time (Fig. 3A), it was prominent that RMSD values of the backbone of NAA10^{F128L} were significantly higher compared to the RMSD values of the backbone of NAA10 (Fig. 3A), indicating the unstable structural properties of NAA10^{F128L} relative to wild-type NAA10. The average RMSD of NAA10 and NAA10^{F128L} were 2.43 Å and 2.91 Å, respectively (Fig. 3A). The simulation data on the radius-of-gyration (R_g) of proteins also showed that the NAA10^{F128L} was structurally less rigid (i.e., more flexible) than the NAA10 over the simulation time (Fig. 3B). Overall, the average R_g values for wild-type NAA10 and NAA10^{F128L} were 159.24 Å and 161.47 Å, respectively (Fig. 3B). The computed line graphs of R_g distribution suggest that the R_g of the majority of wild-type conformers were within a range of 156 Å to 162 Å, whereas the R_g of mutant conformers were broadened within a range of 159 Å to 165 Å (Fig. 3B).

The root mean square fluctuation (RMSF) values associated with the MDSs showed that NAA10^{F128L} exhibited varying residual fluctuation in several regions (Fig. 3C), indicating that NAA10^{F128L} changed its local rigidity in local conformations at several residues. Specifically, the RMSF value of the neighboring residues of L128 of NAA10^{F128L} showed contrasting values than the neighboring residues of F128 of NAA10 (Fig. 3C). Therefore, it was evident that the F128L mutation changed the local structural conformation and local rigidity of the mutation-neighboring region in dynamic conditions. In the NAA10, this region forms helix α5, loop α5-β6, and sheet β6. Although the wild-type NAA10 showed a gradual unfolding of the helix-α5 during the simulation period, NAA10^{F128L} maintained the local rigidity of the α-helical structure of this region during MDS (Figs. 3D, 3E). This preservation of secondary structure helix-α5 in NAA10^{F128L} was correlated with the higher number of intra-molecular hydrogen bonds in the NAA10^{F128L} compared to NAA10 (Fig. 3F).

The helix α5 of NAA10 forms a region that participates in acetyl-CoA binding to NAA10 [16]. The Y122 and T125 of this helix are predictably critical in terms of regulating the guidance and binding of acetyl-CoA to the substrate binding cavity of NAA10. While the relevance of Y122 and T125 of human NAA10 in guiding the binding of acetyl-CoA to the acetyl-CoA-binding cavity of human NAA10 is not experimentally proven, a related study with the NAA10 of *Saccharomyces cerevisiae* (*Sc*NAA10) has shown that the conserved Y165 and T168 residues of *Sc*NAA10 constitute a part of acetyl-CoA binding region of *Sc*NAA10 [16]. The Y165-T168 containing region is speculatively involved in guiding and stabilizing the acetyl-CoA in the acetyl-CoA-binding cavity of *Sc*NAA10. Based on this study, we speculate that the conserved and analogous Y122 and T125 of human NAA10 could also be involved in guiding and mediating the stable binding of acetyl-CoA to the acetyl-CoA-binding cavity of human NAA10. Results suggested that a polar contact between Y122 with F128 in the wild-type NAA10 persisted over the simulation time. This polar interaction was presumed to stabilize the region near F128. Interestingly, no polar contact between Y122 and L128 of NAA10^{F128L} was observed for a considerable time during the MDS. The polar interaction between Y122 and L128 was lost within the 10 ns of simulation. The average intra-residue distance between the carbonyl (C═O) of Y122 and the N-H group of F128 in wild-type NAA10 was 2 Å, whereas the average distance between the C═O group of Y122 and N-H group of L128 in NAA10^{F128L} was increased to 4.8 Å. The local rigidity of the helix-α5 of NAA10^{F128L} induced a hinge (Fig. 3G). Such a hinge allowed the movement of nearby protein regions in such a way that the structural transition blocked the acetyl-CoA binding cavity (Fig. 3H). However, wild-type NAA10 did not show the formation of any hinge region (Fig. 3G), while also showing continuous opening of the acetyl-CoA binding cavity during the simulation time (Fig. 3H).

Overall, the results show that F128, which is located at the beginning of the sheet β6, plays a significant role in correctly positioning the neighboring helix α5 and loop α5-β6 and facilitates the binding of acetyl-CoA. F128L mutation collapses the helix α5 and loop α5-β6 by conformational rigidity, disengaging critical acetyl-CoA binding residues, and blocking the acetyl-CoA binding cavity.

2.4. F128I mutation impairs the flexibility of the substrate binding region of NAA10^{F128I}

Following the understanding of how the F128L mutation modulated the structure of NAA10^{F128L}, we evaluated the effect of F128I mutation on the structure of NAA10^{F128I}. The RMSD values of the backbone of NAA10^{F128I} (with an average RMSD value of 2.66 Å) in MDS were significantly higher than the RMSD values of the backbone of wild-type NAA10 (Fig. 4A). However, the average RMSD value of NAA10^{F128I} was lower than the average RMSD value of NAA10^{F128L} (Fig. 4A), indicating that NAA10^{F128I} was dynamically unstable compared to wild-type NAA10 but more stable than the NAA10^{F128L}. Similar to the NAA10^{F128L}, the NAA10^{F128I} also showed higher R_g values (the average R_g value of NAA10^{F128I} was 161.30 Å) than NAA10 in the MDS (Fig. 4B). Such results indicate less overall structural rigidity of NAA10^{F128I} than NAA10. Therefore, we investigated the impact of F128I mutation on the local conformation changes in NAA10^{F128I}. Comparison of the RMSF values of the residues revealed differences in the flexibility of helix α1, loop α1-α2, and helix α2 of NAA10^{F128I} compared to the wild-type NAA10 (Fig. 4C). The residual fluctuations of these regions were lower in NAA10^{F128I} than in NAA10 (Fig. 4C). Interestingly, the N-terminal loop α1-α2 and C-terminal loop β6-β7 form the substrate peptide binding groove. Hence, the C-terminal mutation near the sheet-β6 (at the 128th position) was speculated to cause low residue fluctuation, thereby impacting the flexibility of the loop α1-α2 of NAA10^{F128I}.

The peaks of the probability distribution function (PDF) of RMSD of proteins show a single conformational state of NAA10 during the trajectory, whereas NAA10^{F128I} showed two major conformations over simulation time (Fig. 4D). The wild-type NAA10 mostly retained the globular conformation (termed as conformation-1) in which the acetyl-CoA binding sites, substrate guiding regions, and substrate binding cavity maintained the structural pattern for conducive binding of acetyl-CoA and substrate proteins/peptides (Fig. 4D). While the NAA10^{F128I} also showed a similar conformation (conformation-1) in the initial phase of simulation, this mutant also existed in an altered conformation (termed as conformation-2) which showed the differential structure of the substrate guiding loops and helices (Fig. 4D). There was an increase of α-helical content in the NAA10^{F128I} during different phases of simulation (Fig. 4E). Specifically, a significant change in the secondary structures occurred at the helix α2 of wild-type NAA10 This α helix structure was converted to a 3_{10}-helix within the initial 100 ns of the simulation (Fig. 4E). On the contrary, conformation-2 of NAA10^{F128I} retained the α-helix structure (Fig. 4E). Additionally, the neighboring region of helix-α2 also preserved the secondary structure in NAA10^{F128I}, whereas the wild-type NAA10 showed wavering secondary structures in the same region. The average number of intra-molecular hydrogen bonds was increased in the helix α1, loop α1-α2, and helix α2 of NAA10^{F128I} (Fig. 4F).

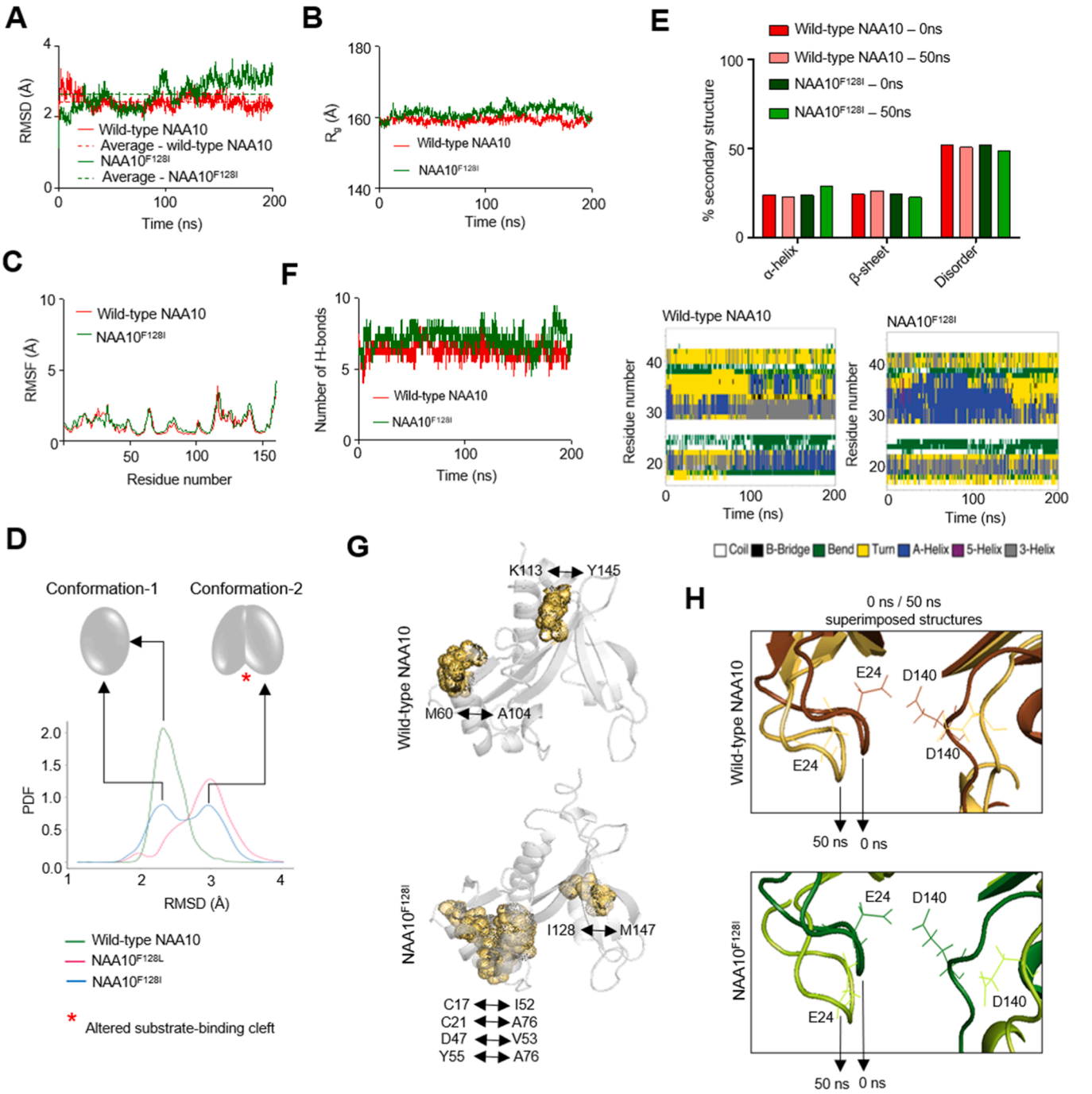

Fig. 4. Steric clashes of I128 lead to the unstable substrate-binding cavity in an alternative conformation of NAA10^{F128I}. (A) Higher RMSD values of the backbone of NAA10^{F128I} compared to RMSD values of the backbone of wild-type NAA10 indicate instability of NAA10^{F128I} during the latter half of the molecular dynamics simulation. (B) Radius of gyration [R_g] of NAA10^{F128I} and NAA10, showing more relaxed and expanded globular structure of NAA10^{F128I} over simulation time. (C) RMSF values of the residues of NAA10^{F128I} and NAA10. Higher RMSF values of substrate-binding residues of NAA10^{F128I} show relative instability of these residues compared to the same residues of wild-type NAA10. (D) NAA10^{F128I} exists in two major conformations during the simulation. (E) Upper panel: analysis of the secondary structure composition of NAA10 and NAA10^{F128I} at 0 ns and 50 ns of simulation shows marginal increase of helical structure in NAA10^{F128I} over the simulation time. Lower panel: secondary structures of substrate-binding region of NAA10 and NAA10^{F128I} during the 200 ns simulation time. (F) The number of intra-molecular hydrogen bonds of α1, loop α1-α2 and α2 of NAA10^{F128I} and NAA10, showing an increase of the H-bonds in the of α1, loop α1-α2 and α2 of NAA10^{F128I} compared to the wild-type NAA10. (G) Residues involved in steric clashes on NAA10 and NAA10^{F128I}. (H) Enlarged superimposed 0 ns and 50 ns structures of the substrate-binding cavities of NAA10 and NAA10^{F128I}. The 50 ns structure of the substrate-binding cavity is unfavorably expanded in NAA10^{F128I} compared to the 50 ns structure of the substrate-binding cavity of NAA10.

The rigidity of the substrate guiding and binding loops and helices of NAA10^{F128I} (conformation-2) resulted in local strain and steric clashes between various residues of NAA10^{F128I} (Fig. 4G) Such steric clashes reoriented the structure of NAA10^{F128I} in such a way that the substrate guiding loop α1-α2 and loop-β6/β7 repositioned themselves significantly distant from each other (Fig. 4H). Such distant positioning of loop α1-α2 and loop β6-β7 is speculated as not being able to coordinately bind the substrate peptides, thereby compromising the substrate acetylation

property of NAA10^{F128I}. On the other hand, NAA10 showed negligible steric clashes between residues (Fig. 4G) which were located far from the substrate guiding loops and helices. Therefore, the relative distance between the loop α1-α2 and loop β6-β7 in NAA10 remained almost conserved during simulation (Fig. 4H), indicating that the loop α1-α2 and loop β6-β7 of NAA10 could remain functional substrate guiding loops throughout the simulation time. Moreover, the helix-to-disorder transition of secondary structures near the helix-α1 and helix-α2 of NAA10 could facilitate the binding of various kinds of substrate peptides (Fig. 4H).

Taken together, these data suggested that F128I mutation occurring near the sheet-β6 caused local conformational changes in the N-terminal helix-α1, loop α1-α2, and helix-α2. Interestingly, the analyses also indicated that the NAA10^{F128I} protein lost flexibility in the N-terminal region, which was in accordance with the dynamicity of the secondary structures in this region. Therefore, the loss of flexibility of such a critical region for substrate peptide binding moved the loop residues distant from the substrate channel, resulting in impaired enzymatic activity of NAA10^{F128I}.

2.5. *Functional validation of the effects of F128L and F128I mutations on the stability and catalytic properties of NAA10^{F128L} and NAA10^{F128I}*

In the concluding phase of our study, we investigated the expression, localization, and function of NAA10^{F128L} and NAA10^{F128I} to decipher their deregulatory functions in IMR32 (neuroblastoma) cells. FLAG-NAA10, as well as its mutants FLAG-NAA10^{F128L} and FLAG-NAA10^{F128I}, exhibited sufficient expression levels within IMR32 cells (Figs. 5A, 5B). However, a significant fraction of NAA10^{F128L} also formed perinuclear aggregates within IMR32 cells (Figs. 5A, 5B). This

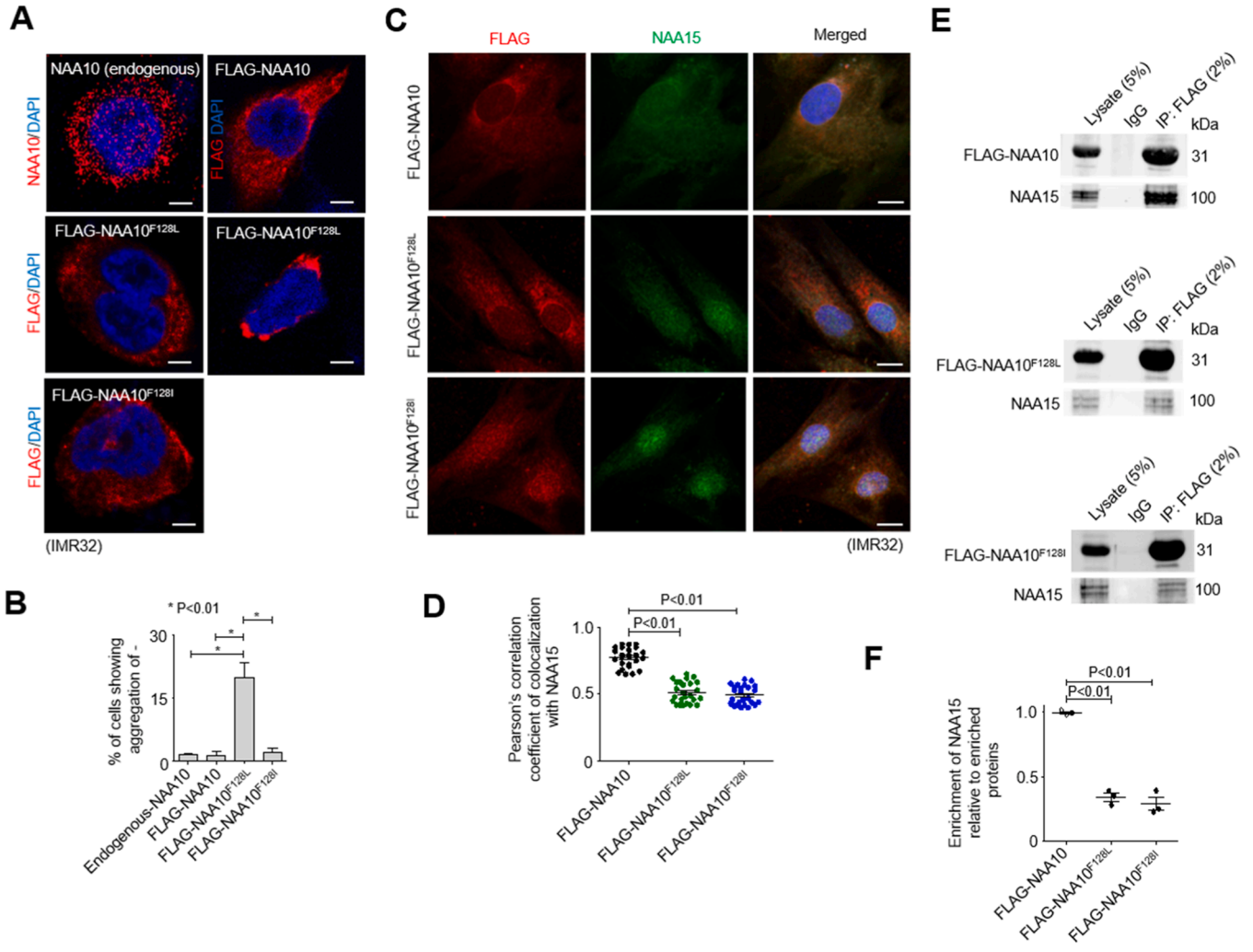

Fig. 5. NAA10^{F128L} and NAA10^{F128I} are stably expressed, but show weak interaction with NAA15. (A) IMR32 cells were untransfected or transfected with clones of FLAG-tagged NAA10, NAA10^{F128L}, and NAA10^{F128I} for 24 h. Representative confocal immunofluorescence microscopy images showing expression of endogenous NAA10, FLAG-NAA10, FLAG-NAA10^{F128L}, and FLAG-NAA10^{F128I}. A significant number of IMR32 cells aggregated FLAG-NAA10^{F128L}. (B) Quantification of cells showing aggregated expression of endogenous NAA10, FLAG-NAA10, FLAG-NAA10^{F128L}, and FLAG-NAA10^{F128I} [100 cells/group in each of three independent experiments]. (C) IMR32 cells were transfected with FLAG-NAA10, FLAG-NAA10^{F128L}, and FLAG-NAA10^{F128I} for 24 h. Representative confocal immunofluorescence microscopy images of colocalization of FLAG-NAA10, FLAG-NAA10^{F128L} and FLAG-NAA10^{F128I} with endogenous NAA15. (D) Quantification of Pearson's correlation coefficient of colocalization of FLAG-NAA10, FLAG-NAA10F128L, and FLAG-NAA10F128I with endogenous NAA15 as represented in 5 C [100 cells/group]. (E) IMR32 cells were transfected with FLAG-NAA10, FLAG-NAA10^{F128L} and FLAG-NAA10^{F128I} for 24 h. Representative immunoblots of FLAG-NAA10, FLAG-NAA10^{F128L}, FLAG-NAA10^{F128I}, and NAA15 from cell lysates with non-denaturing immunoprecipitation of FLAG-NAA10, FLAG-NAA10^{F128L} and FLAG-NAA10^{F128I}. (F) Relative densitometric quantification of the immunoblot bands of NAA15 with respect to immunoblot bands of FLAG-NAA10, FLAG-NAA10^{F128L}, and FLAG-NAA10^{F128I} in the immuno-enriched fractions of FLAG-NAA10, FLAG-NAA10^{F128L}, and FLAG-NAA10^{F128I}. Quantifications are shown as mean ± S.D.; P values are indicated. Scale bar in confocal microscopy images: 5 μm. Microscopy and immunoblot data are representative of at least three independent biological and technical experiments. Each data point of the acetylation assay is the average value of three technical replicates.

suggested that the structural instability of NAA10^{F128L} could potentially trigger its aggregation in physiological conditions.

NAA10^{F128L} and NAA10^{F128I} exhibited colocalization with NAA15 (Figs. 5C, 5D). However, the colocalization of NAA10^{F128L} and NAA10^{F128I} with NAA15 was weaker than the colocalization of wild-type NAA10 with NAA15 (Figs. 5C, 5D), indicating that the F128L and F128I mutations had weakened the association of NAA10^{F128L} and NAA10^{F128I} with the NAA15 in the NatA complex. Considering the interaction between NAA10 and NAA15 in the NatA complex, we further investigated whether the F128L and F128I mutations affected the interaction of NAA10^{F128L} and NAA10^{F128I} with NAA15. Although NAA15 was co-purified with wild-type NAA10, NAA10^{F128L}, and NAA10^{F128I} (Figs. 5E, 5F), the enrichment of NAA15 with NAA10^{F128L} and NAA10^{F128I} was significantly less than the enrichment of NAA15 with wild-type NAA10 (Figs. 5E, 5F), signifying that F128L and F128I mutations altered the potential interactions of NAA15 with NAA10^{F128L} and NAA10^{F128I} in NatA complex.

NAA10 binds to acetyl-CoA during the catalytic transfer of the acetyl group to substrate polypeptides. Our molecular simulation results indicated that the F128L mutation could impede the binding of acetyl-CoA to the ligand binding pocket of NAA10^{F128L}. Consequently, we examined the acetyl-CoA binding abilities of wild-type NAA10, NAA10^{F128L}, and NAA10^{F128I}. While wild-type NAA10 and NAA10^{F128I} exhibited strong interactions with acetyl-CoA, NAA10^{F128L} displayed no such interaction (Figs. 6A, 6B). Notably, the binding affinity of NAA10^{F128I} for acetyl-CoA was weaker than that of wild-type NAA10 (Figs. 6A, 6B). These observations strongly suggested that the F128L mutation abolished the ability of NAA10^{F128L} to interact with acetyl-CoA, whereas the F128I mutation only marginally reduced the potential binding of acetyl-CoA to NAA10^{F128I}.

The microscale thermophoresis (MST) experiments revealed a notable difference in the binding behavior of NAA10^{F128I} compared to NAA10 and NAA10^{F128L} with a small peptide (EEEI-peptide) which was known to be a substrate for NAA10. While both NAA10 and NAA10^{F128L} demonstrated strong binding affinity to the EEA peptide, NAA10^{F128I} lacked significant binding capacity for EEEI-peptide (Fig. 6C). This result underscored that the F128I mutation disrupted the interaction between NAA10^{F128I} and the EEEI-peptide.

We evaluated the in vitro acetylation capacity of wild-type NAA10, NAA10^{F128L}, and NAA10^{F128I} on EEEI-peptide with a previously established experimental procedure [48]. FLAG-NAA10, FLAG-NAA10^{F128L} and FLAG-NAA10^{F128I}-containing NatA complexes were nondenaturing immunopurified from cells that were individually transfected with FLAG-NAA10, FLAG-NAA10^{F128L}, and FLAG-NAA10^{F128I}. FLAG-NAA10/NAA15, FLAG-NAA10^{F128L}/NAA15, and FLAG-NAA10-^{F128I}/NAA15 complexes were incubated with the EEEI-peptide in the presence of [^{14}C]-acetyl-CoA to analyze the capacity of these complexes to acetylate the EEEI-peptide. NatA complexes containing FLAG--NAA10^{F128L} and FLAG-NAA10^{F128I} exhibited significantly reduced N-terminal acetylation activity on the EEEI-peptide compared to the N-terminal acetylation activity of NatA complex containing FLAG-NAA10 on EEEI-peptide (Fig. 6D). The diminished substrate acetylation activity of NatA complex containing FLAG-NAA10^{F128L} might be attributed to its weakened acetyl-CoA binding affinity, while the reduced capacity of NatA complex containing FLAG-NAA10^{F128I} to acetylate the EEEI-peptide could be due to its lower peptide binding ability. Moreover, the NatA-mediated N-terminal acetylation capacity of the F128 variants could have been also reduced due to reduced complex formation with NAA10^{F128L} and NAA10^{F128I} with NAA15, suggesting that the activity of NatA containing NAA10^{F128L} and NAA10^{F128I} might be impaired.

Finally, we examined the N-α-acetylation of Huntingtin (HTT) exon1 by the NatA complex under varying expression conditions of NAA10. To assess N-terminal acetylation, we utilized a mutant construct, HTT25Q exon1^{K6A,K9A,K15A}, where lysine 6, 9, and 15 were mutated to alanine, ensuring that any observed acetylation would reflect N-α-acetylation of HTT25Q exon1^{K6A,K9A,K15A}. This construct was tagged with six contiguous histidine residues at the C-terminus to facilitate affinity purification via Ni^{+2}-NTA.

HTT25Q exon1^{K6A,K9A,K15A} was incubated with [^{14}C]-acetyl-CoA in cell lysates from 293 T cells under different NAA10 expression conditions: (i) endogenous NAA10 expression, (ii) knockout of endogenous *NAA10*, and (iii) ectopic expression of FLAG-tagged wild-type NAA10, FLAG-NAA10^{F128L}, FLAG-NAA10^{F128I}, and a combination of FLAG-NAA10^{F128L}/FLAG-NAA10^{F128I} in endogenous *NAA10*-knockout cells. The data revealed that HTT25Q exon1 in lysates with endogenous NAA10 expression and ectopic wild-type NAA10 expression exhibited robust N-α-acetylation (Fig. 6E). Notably, N-α-acetylation of HTT25Q exon1 in the ectopic wild-type NAA10 expression condition was higher than those in lysates with endogenous NAA10 (Fig. 6E). However, when ectopic expression of mutant NAA10 variants (NAA10^{F128L}, NAA10^{F128I}, or NAA10^{F128L}/NAA10^{F128I}) was introduced in endogenous NAA10 knockout cells, we observed a significant reduction in N-α-acetylation compared to wild-type NAA10 (Fig. 6**E**). These findings demonstrated that the N-α-acetylation capacity of NAA10^{F128L} and NAA10^{F128I} was substantially diminished relative to the wild-type NAA10, highlighting the reduced efficiency of the mutant proteins in acetylating HTT25Q exon1 and possibly other proteins.

In summary, these findings demonstrate that the F128L and F128I mutations alter the abilities of NAA10^{F128L} and NAA10^{F128I} to bind to ligands and substrate peptides without affecting the expression, localization, and NAA15-binding capabilities of the mutant proteins.

3. Discussion

Co-translational and post-translational N-terminal acetylation of nascent polypeptides is catalyzed by a class of conserved enzyme protein complexes (ribosome-bound NatA-NatD mediates co-translation NTA, whereas cytosolic NatF-NatH mediates post-translational NTA) [49]. The substrate-recognition diversity in NATs emphasizes the intricate and specific catalytic nature of Nα-acetylation, highlighting the complexes' significant role in shaping the spatial and functional properties of the human proteome. N-terminal acetylation influences diverse protein functions, impacting protein folding, stability, complex formation, and cellular localization. Therefore, the spatial and temporal catalytic activity of NAA10 is significantly important in the overall process of proteostasis. Consequently, Ogden syndrome, characterized by postnatal growth failure, severely delayed psychomotor development, variable dysmorphic features, hypotonia, and cardiac arrhythmias, result from pathogenic *NAA10* mutations. In Ogden syndrome, neurological symptoms include cerebral atrophy, microcephaly, seizures, and hypotonia progressing to hypertonia, often accompanied by severe intellectual disability and nonverbal communication (Supporting table ST2). Microphthalmia in individuals with Ogden syndrome is also reported. Cardiac abnormalities, including arrhythmias, septal defects, and hypertrophic cardiomyopathy, are common and frequently lead to early death in males due to heart failure. Other features include feeding difficulties, skeletal anomalies, visual impairments, and conductive hearing loss. Death typically occurs in early childhood, often before the age of 2 in males, primarily due to cardiac complications. Notably, many of females with Ogden syndrome show phenotypic overlap and specific traits with the males, and some of the females with Ogden syndrome survive to adulthood [39, 42]. It has been suggested that Ogden syndrome is a phenotypic spectrum of one disease, while it is also suggested that the entire disease can be referred to interchangeably as Ogden syndrome or NAA10-related neurodevelopmental syndrome. Deciphering the structural and functional perturbation of NAA10 due to mutations is of paramount importance in mechanistic understanding of the catalytic inactivation of NAA10 in diseases.

Our study provided a robust analysis to simultaneously evaluate the disease-associated missense mutations' impact on key properties of the NAA10's stability and function. The analyses indicated that studying the

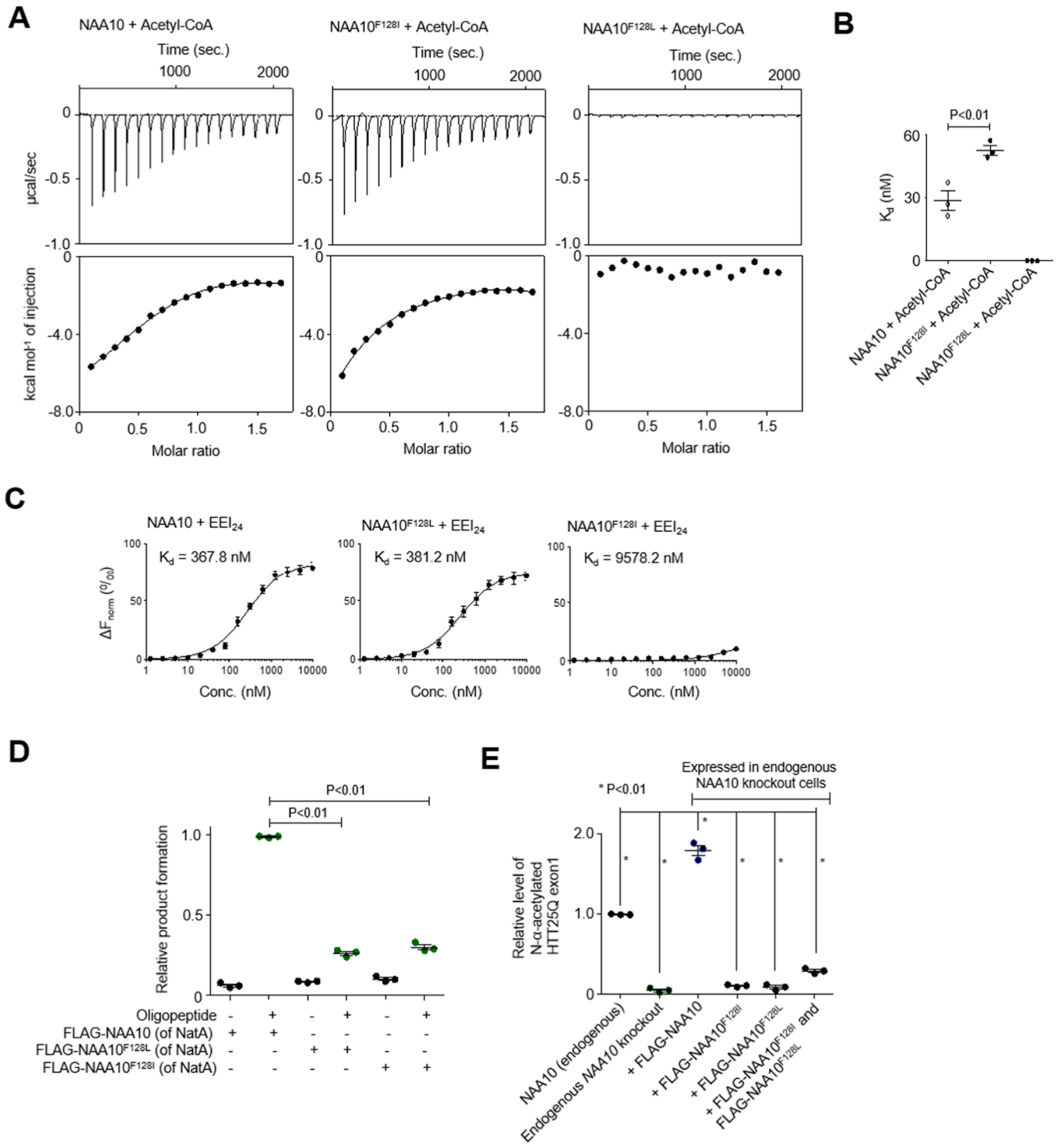

Fig. 6. NAA10^{F128L} and NAA10^{F128I} are catalytically inactive due to lack of acetyl-CoA and substrate-binding capacities, respectively. (A) Left: representative quantification of binding of NAA10, NAA10^{F128L}, and NAA10^{F128I} with acetyl-CoA by isothermal titration calorimetry. (B) Dissociation constant [K_d] values measured in three independent experiments. (C) Microscale thermophoresis-based experiments of NAA10, NAA10^{F128L,} and NAA10^{F128I} binding to EEEI-peptide. Dissociation constant [K_d] values are given. (D) In solution acetylation assay of EEEI-peptide by anti-FLAG immunopurified NatA complexes containing FLAG-NAA10 or FLAG-NAA10^{F128L} or FLAG-NAA10^{F128I}, showing significantly less capacity of NatA complexes containing FLAG-NAA10^{F128L} and FLAG-NAA10^{F128I} in acetylating EEEI-peptide compared to ability of NatA complex containing FLAG-NAA10 to acetylate EEEI-peptide. (F) N-α-acetylation of recombinant HTT25Q exon1 protein in lysates of cells expressing endogenous NAA10, *NAA10* knockout cells, *NAA10* knockout cells ectopically expressing wild-type NAA10, NAA10^{F128L}, NAA10^{F128I}, and combination of NAA10^{F128L}/NAA10^{F128I}. N-α-acetylation of recombinant HTT25Q exon1 is significantly lower in *NAA10* knockout cells and in *NAA10* knockout cells expressing NAA10^{F128L}, NAA10^{F128I}, NAA10^{F128L}/NAA10^{F128I} compared to N-α-acetylation of recombinant HTT25Q exon1 in endogenous and ectopic wild-type NAA10 expressing cells. Quantifications are shown as mean ± S.D.; P values are indicated. Experimental data are representative of at least three independent biological and technical experiments.

F128L and F128I mutations of *NAA10* among the fifteen known mutations is paramount due to their significant impact on both the structural integrity and functional regulation of the protein. On the contrary, other mutations in NAA10 [37, 38, 42–44, 50, 51] either cause structural destabilization or functional inactivation, but not both at the same time. Therefore, F128L and F128I mutations, occurring at conserved sites, demonstrate a crucial role in destabilizing the structure-function association of NAA10. The substitution of the aromatic amino acid at the 128th position with small aliphatic amino acids affects the local stability of the region, as indicated by lower interaction energies with neighboring residues compared to the wild-type. Moreover, these mutations are located within a sequence motif critical for binding to other proteins, thereby suggesting potential alterations in protein-protein interactions and phosphorylation status. Additionally, conservation analysis underscores the irreplaceability of the amino acid at position 128, emphasizing the unfavorable consequences of these mutations on NAA10's structural and functional landscape. Integration of various analyses identifies F128L and F128I as particularly destabilizing both the structure and function of NAA10, making it a focal point for understanding the molecular mechanisms underlying NAA10-related neurodevelopmental syndromes. We identified F128L and F128I mutations as most detrimental to NAA10′s structural and enzymatic properties, as experimental evidence underscored the mutations' capacity to alter the catalytic activity of $NAA10^{F128L}$ and $NAA10^{F128I}$ by modulating these proteins' interactions with substrate peptide and acetyl-CoA.

F128 residue can be considered as a structural hub, as it is connected to several other residues by nodes of hydrogen bonds, aromatic and hydrophobic interactions, and Van Der Waals forces. Substitution of the phenylalanine residue by other amino acids at the 128th position of NAA10 is energetically unfavorable due to loss of interactions and folding anomalies.

F128 is a conserved residue located at the end of loop α5–β6, pointing inward in a hydrophobic pocket between β4, α3, β5, α4, and β7 of NAA10. As such, F128 is a non-catalytic and non-substrate guiding residue present in a hydrophobic pocket outside the functionally relevant regions of the NAA10. However, F128L and F128I mutations are classic examples of how the mutations of a non-catalytic residue can cause the catalytic collapse of an enzyme in different mechanisms. In the hydrophobic pocket, F128 interacts with M91, V107, L109, Y122, M147, K148, and R149. Besides the π-stacking interaction with Y122, the F128 participates in hydrophobic interactions with the non-polar side chains of residues of the cleft. The closest distance between the F128 and its interacting residues is in the range of 2.3 – 3.7 Å. Since this distance range is within the optimum limits of hydrophobic and van der Waals interactions, the extent of the hydrophobic zone created by the extended hydrophobicity of bulky F128 is required to stabilize the hydrophobic pocket. Substitution of F128 with smaller aliphatic amino acids (such as leucine and isoleucine) reduces the 128th residue's side chain length in such a way that the average distance between these residues (L128 and I128) and other hydrophobic amino acids of the groove exceeds the limits of hydrophobic interactions. The simulation-based calculations showed that the average distance between L128/I128 and other residues of the groove was in the range of 5.1 – 13.9 Å. Therefore, several events in the molecular simulation showed the loss of hydrophobic interactions of L128/I128 with other hydrophobic residues. Although leucine and isoleucine are highly hydrophobic, the lower distance range of hydrophobicity of L128 or I128 can be accounted for the loss of hydrophobic interactions in the concerned region. It is also pertinent to note that the F128 is the central residue that holds other hydrophobic residues by simultaneously connecting with them in the groove. No other residue in that groove shows such high node connectivity to play a decisive role in the maintenance of the groove structure and topology. Therefore, mutation of F128 with leucine or isoleucine will tend to deform and destabilize the hydrophobic groove. Indeed, this groove harboring L128 or I128 in $NAA10^{F128L}$ and $NAA10^{F128I}$ collapsed at several time points of simulations. Overall, the effect of structural changes of the L128/I128 groove is propagated to impact the stability of acetyl-CoA and substrate peptide binding residues.

Our findings reveal that the wild-type and mutant NAA10 proteins (F128I and F128L) exhibit diverse folding patterns. Although the F128I and F128L mutations have similar global effects in altering the NAA10 structure, they exhibit distinct local conformational changes. In $NAA10^{F128I}$, the region encompassing the N-terminal helix α1, loop α1–α2, and helix α2 exhibits reduced flexibility, thereby conciliating the interaction of substrate peptide binding groove to C-terminal loop β6-β7 of NAA10. Interestingly, the essential dynamics analyses showed divergent motion between the loop α1–α2 and the loop β6-β7, strongly validating the experimental evidence of compromised substrate peptide binding to NAA10, ultimately leading to the functional impairment of $NAA10^{F128I}$. Conversely, in $NAA10^{F128L}$, helix α5 and loop α5-β6 (corresponding to the region with two important acetyl-CoA-interacting residues, Y122 and T125) are less flexible. Therefore, the F128L mutation disrupts the backbone interaction between Y122 and the L128 residue of the $NAA10^{F128L}$, leading to impaired binding of acetyl-CoA to $NAA10^{F128L}$ and loss of function of $NAA10^{F128L}$.

An interesting question is why the F128L and F128I mutations differentially alter the local structures of acetyl-CoA binding and substrate binding regions. Although having similar hydrophobicity, the different effect of 128th leucine and isoleucine on NAA10 structure relies on the variability of side chain properties of these two amino acids. The side chain leucine at the 128th position of $NAA10^{F128L}$ creates a hinge in the backbone. The hinge changes the relative dynamicity of the upstream and downstream regions of L128. Such a motion perturbed the proximal patches of local structures (such as the acetyl-CoA binding region) but did not show a distant effect on the structural rigidity of the substate-binding region. On the contrary, I128 of $NAA10^{F128I}$ does not induce a large relative motion of regions. The steric clash effect of I128 is limited to distant regions, mostly affecting the activity and stability of substrate peptide-binding residues. In general, we speculate that a bulky side chain, such as found in phenylalanine and isoleucine, at the 128th position is required to prevent the hinge and gross intramolecular dynamic motion of the NAA10 backbone. Therefore, the observed decreased flexibility of $NAA10^{F128L}$ in the vicinity of the mutated residues, especially in regions crucial for acetyl-CoA binding, and the divergent motion of substrate peptide binding loops of $NAA10^{F128I}$ suggest a nuanced impact on the protein's binding to acetyl-CoA and its substrate peptide, respectively.

Although NAA15 showed colocalization and enrichment with $NAA10^{F128L}$ and $NAA10^{F128I}$, it was observed that the colocalization and enrichment of NAA15 with $NAA10^{F128L}$ and $NAA10^{F128I}$ was significantly weaker than the colocalization and enrichment of NAA15 with wild-type NAA10, indicating a weaker association of $NAA10^{F128L}$ and $NAA10^{F128I}$ with NAA15 in NatA complex.

In conclusion, the findings of this study shed light on the intricate relationship between specific mutations of non-catalytic residues and the consequential alterations in the NAA10's structural and enzymatic properties, offering valuable insights into the mechanistic details of pathogenic NAA10 mutations.

4. Methods and materials

4.1. Data

Disease-associated mutations of NAA10 were curated from the HGMD database [52]. The structure of the NAA10 was obtained from the RCSB Protein Data Bank (PDB: 6PW9, chain C) [53].

4.1.1. Protein structure

The F128L and F128I mutations in the structure of NAA10 were generated using the Mutagenesis wizard of Pymol with the best-oriented rotamer of residues at position 128. The model structures of $NAA10^{F128L}$ and $NAA10^{F128I}$ were checked and validated in MolProbity [54], and the

Ramachandran plots of both structures were checked.

4.1.2. Protein structure network analysis

Protein structure network (PSN) analysis was performed using the residue interaction network implemented in RING2.0 [55]. The residues that had at least five edges were considered hubs, and the nodes were considered to represent the interconnected residues in the closest network policy. In the contact-based PSN, we defined the cutoff values for each type of interaction as follows- salt bridges: 5 Å, hydrogen bonds: 5.5 Å, van der Waals (VDW) interactions: 0.8 Å, π-π stacking: 7 Å, π-cation interaction: 7 Å, and disulfide bond: 3 Å. For the hydrogen bonds, the limiting angle between the donor-acceptor pair was set to 63°, while the VDW interaction was limited to carbon-carbon and carbon-sulfur atoms only. The distance estimate was based on the center of mass of the side chains of residues.

4.1.3. Folding free energy analysis for protein stability

The FoldX [56] energy function was used to determine the difference in folding free energy (ΔΔG) of different point mutants of NAA10 and wild-type NAA10. A negative ΔΔG indicates destabilizing changes in folding free energy by the mutation.

4.1.4. Short linear interaction motif analysis

The short linear interaction motifs (SLiMs) in NAA10 protein were annotated using the Eukaryotic Linear Motif (ELM) server compilation database [57]. The SLiMs that corresponded to interaction of non-cytosolic proteins with NAA10 were not considered. We analyzed the occurrence of different NAA10 mutations on SLiM.

4.1.5. Analysis of changes in posttranslational modifications

We manually curated the post-translational modifications (PTMs) at the different mutations and the regions of NAA10 adjacent to the mutation. We also identified the predicted changes in mutation-associated PTMs by the MutPred algorithm [58].

4.1.6. Sequence conservation analysis

The Gremlin program [59] was used to understand amino acid conservation and coevolution. The conservation score for the NAA10 sequence of 27 organisms (both plants and animals) measured the linkage matrix of amino acids of wild-type NAA10 of different organisms. The residues with a bit score of at least 1 are considered conserved.

The sequences of NAA10 of different organisms were also acquired from the National Center for Biotechnology Information (NCBI) protein database. The alignments of sequences were done in Clustal Omega [60].

4.1.7. Predictive pathogenicity analysis of mutations

The predictive pathogenicity associated with each missense mutation of NAA10 was analyzed using the PolyPhen-2 score [61], a predictive value derived from the substitution of amino acids on protein structure and function. PolyPhen-2 scores ranged from 0 to 1. Based on specificity and sensitivity, scores > 0.5 indicate strong pathogenicity potential, whereas scores below 0.5 were considered benign. Pathogenicity scores of each mutation was also analyzed by CADD and REVEL.

4.1.8. Molecular dynamics simulation (MDS)

The molecular dynamics simulation (MDS) was done as described in our previous studies [62, 63]. Overall, the MDS of wild-type and mutant protein structures were carried out using GROMACS (version 2018.8). The force field parameters were calculated based on the OPLS-AA/L all-atom force field (2001 amino acid dihedrals). The simulation environments for the proteins were created by solvating the structures in a transferable intermolecular potential 4 P (TIP4P) water model up to 20 Å from the protein structures in a cubical geometry. Next, the sodium and chloride ions were added to the solvent to neutralize the charged residues of the protein. Periodic boundary condition was used in all dimensions. Solvated structures were minimized using the steepest descent method till the system attained a convergence threshold of < 1000.0 kcal/mol [64–66]. Next, pre-simulation equilibrating steps comprised of constant NVT and constant NPT (N = number of particles, V= volume, T = absolute temperature, P = pressure) conditions with restraints on the heavy atoms of the protein were carried out. Finally, an unrestrained 200 ns full simulation was performed, followed by the equilibration.

Root mean square deviations (RMSD) of protein backbones, root-mean-square fluctuations (RMSF) of the amino acid residues and the radius of gyrations (R_g) of the proteins were generated by using "gmx rms", "gmx rmsf", and "gmx gyrate" functions respectively. The number of intramolecular hydrogen bonds and the distance between two atoms were calculated using the "gmx hbond" and "gmx distance" functions, respectively. The simulation trajectory files were read, and the secondary structures for each time frame were computed using "gmx do_dssp" by calling the dssp program.

4.1.9. Essential dynamics analysis

Dominant motions in the simulation systems were analyzed through essential dynamics analysis of the trajectory files. The covariance matrix of atomic coordinates, including their eigenmodes, was calculated. Subsequently, the extracted data for the matrix was diagonalized using "gmx covar", yielding the diagonal matrix of the eigenvectors. Next, "gmx anaieg" was used to analyze eigenvectors, and the first two eigenvectors, which contain the substantial dominant motion, were plotted oppositely in phase space.

The free energy (FE) landscape which represents the Gibbs free energy of the conformations of proteins through the trajectory, was plotted with the first two principal components obtained from previous analyses using the "gmx sham" function.

Dynamical cross-correlation maps were generated for the simulation systems to analyze the pairwise shift of the Cα atoms of the proteins. Changes in the coupled atomic displacement can provide information about the impact of mutations on protein dynamics. Using the bio3d package of R programming, the correlations (C_{ij}) between Cα atoms of the proteins were calculated and displayed in a graphical representation. The C_{ij} values range from −1 (complete anti-correlation) to + 1 (complete correlation). The positive values denote correlated motion in the same direction, and the negative values represent correlated motion in the opposite direction. The value of C_{ij} implies the strength of the correlation between atoms.

4.1.10. Web-servers

Secondary structure analysis: 2Struc [67], steric clash analysis: Molprobity [68], analysis of hinge regions in proteins: HingeProt [69].

4.1.11. Cloning

The overall process of gene cloning was done as described in our previous studies [70, 71]. Briefly, total mRNA was isolated from IMR32 cells using RNA extraction kit [ThermoFischer Scientific (TFS), 12183018 A], followed by the generation of cDNA pool from the mRNAs using oligo-dT (Eurofin genomics) primer and reverse transcription. The ORF of *NAA10* was amplified from the cDNA pool by polymerase chain reaction (TFS, Phusion™ High-Fidelity DNA Polymerase, F-530XL) using primer sets listed in Table 1. The PCR product of NAA10-ORF and plasmid vectors were restriction digested by restriction enzymes [New England Biolabs (NEB)], followed by ligation of the restriction digested products by T4 DNA ligase (NEB, M0202S). The ligated products were transformed into the ultracompetent DH5α strain of *Escherichia coli*, followed by the selection of positive clones in antibiotic-containing selective growth medium and colony PCR (Takara Bio, RR350A). The HTT25Q exon1 clones was used from our earlier studies [72, 73] All the clones were sequences at the Research Support Service Group of CDFD. The list of clones and vectors is given in Table 1.

Table 1
Clones and oligos.

Clone name	Vector	Primer type	Sequence	Restriction site
NAA10-pET21b	pET21b	Forward	GGAATTCCATATGAACATCCGCAATGCGAGGCCA	*Nde*I
		Reverse	CCCAAGCTTGGAGGCTGAGTCGGAGGCCTCT	*Hind*III
NAA10-pcDNA3.1 +	pcDNA3.1 + (FLAG)	Forward	CTAGCTAGCATGAACATCCGCAATGCGAGGC	*Nhe*I
		Reverse	GGGGTACCGGAGGCTGAGTCGGAGGCCT	*Kpn*I
SDM_F128I	pcDNA3.1 + (FLAG-NAA10)	Forward	CACCCTCAAC**a**ttCAGATCAGTG	-
		Reverse	TTGGAATAGAGGTGCAG	-
SDM_F128L	pcDNA3.1 + (FLAG-NAA10)	Forward	CACCCTCAAC**tt**gCAGATCAGTG	-
		Reverse	TTGGAATAGAGGTGCAG	-

4.1.12. Site-directed mutagenesis

The c .384 T > A and c .384 T > G mutations in the ORF of *NAA10* was introduced by NEB Q5 site-directed mutagenesis kit using manufacturer's protocol and the oligos listed in Table 1.

4.1.13. Recombinant protein production and purification

Recombinant NAA10, NAA10^{F128L}, NAA10^{F128I}, and HTT25Q exon1 were separately expressed by T7 expression system as described in our previous studies [74]. Briefly, the pET21b vector bearing the clones of NAA10, NAA10^{F128L} and NAA10^{F128I} were transformed into the BL21 (DE3) strain of *Escherichia coli*. Positive colonies were inoculated in LB-ampicillin medium for 4 h to make the primary culture, followed by expansion of primary culture to secondary culture. Recombinant protein production was induced in secondary culture by incubating the culture with 1 mM isopropyl-β-D-thiogalactoside [Sigma Aldrich (SA), I6758] for 12 h at 37 °C with 180 rpm. Subsequently, bacterial cells were harvested by centrifugation at 5000 rpm for 5 min, followed by lysis of the cells in ice-cold lysis buffer [50 mM Tris-Cl (pH: 8.0), 300 mM NaCl, 10 mM imidazole, 1 mM PMSF (SA, P7626)] for 30 min. Cell lysis was completed by sonication, followed by clearing of cell lysate by centrifugation at 14000 rpm, 4 °C for 40 min. The supernatant of cell lysate was passed through a column of charged Ni^{+2}-NTA beads. Protein-bound Ni^{+2}-NTA beads were rigorously washed with wash buffer [50 mM Tris-Cl (pH: 8.0), 300 mM NaCl, 40 mM imidazole], followed by elution of the recombinant proteins in elution buffer [50 mM Tris-Cl (pH: 8.0), 300 mM NaCl, 300 mM imidazole]. Eluted proteins were dialyzed in specific dialysis buffer (as required in downstream experiments) using fast protein liquid chromatography.

4.1.14. Isothermal titration calorimetry

Bindings of acetyl-CoA to NAA10, NAA10^{F128L}, and NAA10^{F128I} were measured by isothermal titration calorimetry (ITC) studies as described in our earlier study [75]. ITCs were done in a MicroCal ITC instrument (Malvern Panalytical) with the following parameters – protein concentration: 10 μM, acetyl-CoA concentration: 100 μM, total binding events: 18 (the first binding event was the calibration event and not presented in the binding graphs), syringe speed: 180 rpm, power reference: 10 μcal/s, temperature: 25 °C.

4.1.15. In vitro acetylation assay

In vitro N-α-acetylation of EEEI$_{24}$ peptide: The NatA complexes containing the FLAG-NAA10, FLAG-NAA10^{F128L}, and FLAG-NAA10^{F128I} were immunopurified by anti-FLAG antibody from lysate of cells which were separately transfected with FLAG-NAA10, FLAG-NAA10^{F128L} and FLAG-NAA10^{F128I}. 250 μg of immunopurified NatA complex containing NAA10 or NAA10^{F128L} or NAA10^{F128I} was separately incubated with 50 μM [^{14}C]-acetyl-CoA [10 μCi (370 kBq); PerkinElmar] and 200 μM oligopeptide EEEI$_{24}$ (EEEIAALRWGRPVGRRRRPVRVYP) (BioGenes) in the acetylation buffer [20 mM Tris–HCl (pH 8.0), 1 mM EDTA, 15 % glycerol) at 37 °C for 30 min. Negative control experiments lacked oligopeptide. Reactions were stopped by heating the suspensions at 95 °C for 5 min, followed by drop-casting the total reaction suspension (30 μl) onto a P81 phosphocellulose filter paper (Millipore). Filter discs were mildly washed with 10 mM HEPES buffer (pH 7.4) and air-dried. Dried filter discs were immersed in Ultima Gold F scintillation cocktail (PerkinElmer) for 2 min, followed by determining the radioactivity count of samples in TRI-CARB 4910TR 110 V Liquid Scintillation Counter (PerkinElmar).

In vitro N-α-acetylation of HTT25Q exon1: 293 T cells expressing endogenous NAA10, *NAA10* knockout 293 T cells, and *NAA10* knockout 293 T cells ectopically expressing wild-type NAA10, NAA10^{F128L}, NAA10^{F128I}, or both NAA10^{F128L} and NAA10^{F128I}, were lysed separately in NP40 lysis buffer [50 mM Tris (pH 7.4), 150 mM NaCl, 1 % Nonidet P-40]. The lysates were cleared by centrifugation at 5000 rpm for 20 min at 4 °C. 500 μg of total protein from each lysate was incubated individually with 50 μM of freshly prepared, dialyzed recombinant HTT25Q exon1 and 50 μM [^{14}C]-acetyl-CoA [10 μCi (370 kBq); PerkinElmer] in acetylation buffer [20 mM Tris–HCl (pH 8.0), 15 % glycerol] at 37 °C for 30 min. The reactions were terminated by heating the suspensions at 95 °C for 5 min. HTT25Q exon1 was then purified from each reaction condition using Ni^{2+}-NTA column chromatography, as described in the previous section. The eluted HTT25Q exon1 suspensions were concentrated using a centrifugal concentrator with an Ultracel membrane (Amicon Ultra Centrifugal Filter, 3 kDa MWCO; Millipore; UFC900308) to a final volume of approximately 50 μl. The entire suspension (50 μl) was drop-cast onto P81 phosphocellulose filter paper (Millipore). The filter discs were gently washed with 10 mM HEPES buffer (pH 7.4) and air-dried. Finally, the dried filter discs were immersed in Ultima Gold F scintillation cocktail (PerkinElmer) for 2 min, and the radioactivity of the samples was measured using a TRI-CARB 4910TR Liquid Scintillation Counter (PerkinElmer).

4.2. Microscale thermophoresis analysis of protein-peptide interaction

Recombinant NAA10, NAA10^{F128L}, and NAA10^{F128I} were labeled with Monolith NT Protein Labeling Kit RED (NanoTemper Technologies) in a compatible buffer [50 mM Tris-Cl (pH: 7.2), 150 mM NaCl, 10 mM $MgCl_2$] following the manufacturer's protocol. Microscale thermophoresis (MST) analyses for binding of EEEI$_{24}$ (EEEIAALRWGRPVGRRRRPVRVYP) oligopeptide (BioGenes) with NAA10, NAA10^{F128L} and NAA10^{F128I} were done by individually titrating 20 nM of NAA10, NAA10^{F128L} and NAA10^{F128I} with 1:1 EEEI$_{24}$ dilutions (concentration of EEEI$_{24}$ was in range of 1.25 – 10,000 nM). MST of binding assays were done in standard capillaries (NanoTemper Technologies) on a Monolith NT.115 system (NanoTemper Technologies) using 50 % LED and 20 % IR-570 laser power [laser timing: 30 s on/5 s off]. The fluorescence values were normalized, and dissociation constant values (K_d) were analyzed in GraphPad-Prism.

4.2.1. Cell culture and transfection

IMR32 and 293 T cells were acquired from the National Centre for Cell Sciences (NCCS, India). Endogenous *NAA10* knockout 293 T cells were obtained from Applied Biological Materials (ABM, 31365141). Although cells were not genotyped, they were phenotypically characterized with the morphology and shapes properties. Cells were cultured in advanced DMEM medium (TFS, 12,491,023) that was supplemented with 10 % fetal bovine serum (TFS, 26,140,095), 2 mM L-glutamine (TFS, 25,030,164) and 1x antibiotic-antimycotic solution (TFS,

11,548,876). Cells were optimally grown in a humified static incubator that maintained 37 °C and 5 % CO_2 level. Cells were regularly checked for mycoplasma contamination using Venor™ GeM mycoplasma detection kit [SA, MP0025].

Mammalian expression vector (pcDNA3.1)-containing NAA10, $NAA10^{F128L}$, and $NAA10^{F128I}$ clones were transfected into the IMR32 or *NAA10* knockout 293 T cells using lipofectamine-2000 (TFS, 11,668,019) and Opti-MEM (TFS, 31,985,070) medium following manufacturer's protocol.

4.2.2. Immunoprecipitation and immunoblotting

Immunoprecipitation: Nondenaturing immunoprecipitations were done by incubating 2 mg of protein from the lysate of transfected cells with anti-FLAG antibody (listed in Table 2) using crosslink magnetic IP/co-IP method [TFS (Pierce Crosslink 632 Magnetic IP/co-IP kit), 88805) following the manufacturer's protocol.

Immunoblotting: 60 μg of protein was mixed with 4x Laemmli buffer (Bio-Rad, 161–0747) and the suspension was heated at 95 °C for 10 min. Proteins were run on a 12 % SDS-polyacrylamide gel for separation, followed by the transfer of the proteins from the gel to a polyvinylidene fluoride (PVDF) membrane (Amersham 638 Hybond P 0.45, GE Healthcare Life Sciences). The protein-containing membrane was blocked by 5 % skim milk solution (in TBS), followed by incubation of the membrane with primary and secondary antibodies (listed in Table 2). The membrane was intermittently washed with TBST. The chemiluminescent signal was generated by SuperSignal west femto maximum sensitivity substrate (TFS, 34094) and detected by ChemiDoc XRS+ imaging system (Bio-Rad). Densitometric quantification of bands was done in ImageJ2 software.

4.2.3. Immunocytochemistry and microscopy

Untransfected and transfected cells were grown on a glass cover slip (Bluestar). Cells were washed with PBS, followed by incubation with 0.2 % Triton-X 100 solution (in PBS) for permeabilization. Permeabilized cells were fixed with 4 % paraformaldehyde solution (in PBS), followed by blocking with 1 % bovine serum albumin solution (in PBS). Subsequently, cells were subjected to primary and secondary antibodies (listed in Table 2) at room temperature for 2 h in a shaker (40 spm). Cells were intermittently washed with PBS several times. Cells were mounted in prolonged antifade gold with or without DAPI (TFS, P36931; P10144). Images were captured in LSM700 confocal laser scanning microscope (Carl Zeiss) with the 63x Plan652 Apochromat/ 1.4 NA oil/ DIC M27 objective.

Image processing and analysis were done in Zen-Lite 2010 software (Carl 653 Zeiss).

Pearson's correlation coefficient of colocalization of proteins was determined in the Coloc 2 of Image J (Fiji). The number of aggregates of proteins in cells was manually counted.

4.2.4. Statistical analysis

The statistical significance of the difference of means between groups was analyzed by two-tailed, homoscedastic student's t-test. $P < 0.05$ represented a statistically significant difference.

Table 2
Antibodies.

Primary antibodies			
Target protein	Species	Supplier	Catalogue number
FLAG	Mouse	Sigma Aldrich	F3165
NAA10	Rabbit	ThermoFischer Scientific	PA5 −32236
NAA15	Rabbit	ThermoFischer Scientific	PA5 −118509
Secondary antibody (immunoblotting)			
anti-rabbit IgG (whole molecule) peroxidase antibody	Goat	Sigma-Aldrich	A0545
Secondary antibodies (immunocytochemistry)			
anti-Mouse IgG (H+L)- Alexa Fluor Plus 555	Goat	ThermoFischer Scientific	A32727
anti-Rabbit IgG (H+L)- Alexa Fluor Plus 488	Goat	ThermoFischer Scientific	A32731
Anti-Rabbit IgG (H+L)- Alexa Fluor Plus 555	Goat	ThermoFischer Scientific	A32732

Funding

Research in the CFG group is supported by core research funding of CDFD and a grant from the Department of Biotechnology (grant number: BT/PR45460/MED/12/952/2022), Government of India. SS is supported by the junior and senior research fellowships of the Council of Scientific and Industrial Research (CSIR) of the Government of India.

CRediT authorship contribution statement

Smita Saha: Writing – original draft, Methodology, Investigation, Formal analysis, Data curation, Conceptualization. **Akash Ranjan:** Writing – original draft, Validation, Supervision, Resources, Project administration, Funding acquisition, Formal analysis, Conceptualization. **Debasish Kumar Ghosh:** Writing – original draft, Validation, Supervision, Software, Project administration, Formal analysis, Data curation, Conceptualization. **Buddhi Prakash Jain:** Methodology, Investigation, Formal analysis.

Declaration of Competing Interest

The authors declare that they have no known competing financial interests or personal relationships that could have appeared to influence the work reported in this paper.

Acknowledgments

The authors are thankful to the members of the Computational and Functional Genomics (CFG) group for their helpful comments on the study and manuscript. The authors also thank Chilakala Gangi Reddy for his help in the simulation studies.

Appendix A. Supporting information

Supplementary data associated with this article can be found in the online version at doi:10.1016/j.csbj.2024.11.014.

Data Availability

All the data related to the study are provided in the manuscript. The resources and protocols used in this study are available from the corresponding author upon request.

References

[1] Wang X, et al. Posttranslational modification and quality control. Circ Res 2013;112(2):367–81.
[2] Millar AH, Heazlewood JL, Giglione C, Holdsworth MJ, Bachmair A, Schulze WX. The scope, functions, and dynamics of posttranslational protein modifications. Annu Rev Plant Biol 2019;70:119–51.
[3] Sadowska-Bartosz I, Bartosz G, Grune T, Sereikaite J. Role of oxidative, nitrative, and chlorinative protein modifications in aging and age-related diseases. Oxid Med Cell Longev 2018;2018:3267898.
[4] Dyda F, Klein DC, Hickman AB. GCN5-related N-acetyltransferases: a structural overview. Annu Rev Biophys Biomol Struct 2000;29:81–103.
[5] Guzman UH, Aksnes H, Ree R, Krogh N, Jakobsson ME, Jensen LJ, et al. Loss of N-terminal acetyltransferase A activity induces thermally unstable ribosomal proteins and increases their turnover in Saccharomyces cerevisiae. Nat Commun 2023;14:4517.
[6] Aksnes H, Drazic A, Marie M, Arnesen T. First Things First: Vital Protein Marks by N-Terminal Acetyltransferases. Trends Biochem Sci 2016;41:746–60.

[7] Forte GM, Pool MR, Stirling CJ. N-terminal acetylation inhibits protein targeting to the endoplasmic reticulum. PLoS Biol 2011;9:e1001073.
[8] Arnesen T. Towards a functional understanding of protein N-terminal acetylation. PLoS Biol 2011;9:e1001074.
[9] Hwang CS, Shemorry A, Varshavsky A. N-terminal acetylation of cellular proteins creates specific degradation signals. Science 2010;327(5968):973–7.
[10] Linster E, et al. Cotranslational N-degron masking by acetylation promotes proteome stability in plants. Nat Commun 2022;13(1):810.
[11] Mueller F, et al. Overlap of NatA and IAP substrates implicates N-terminal acetylation in protein stabilization. Sci Adv 2021;7(3).
[12] Varland S, et al. N-terminal acetylation shields proteins from degradation and promotes age-dependent motility and longevity. Nat Commun 2023;14(1):6774.
[13] Mullen JR, et al. Identification and characterization of genes and mutants for an N-terminal acetyltransferase from yeast. EMBO J 1989;8(7):2067–75.
[14] Arnesen T, et al. Identification and characterization of the human ARD1-NATH protein acetyltransferase complex. Biochem J 2005;386(Pt 3):433–43.
[15] Gottlieb L, Marmorstein R. Structure of human natA and its regulation by the huntingtin interacting protein HYPK. Structure 2018;26:925–35. e8.
[16] Deng S, et al. Structure and mechanism of acetylation by the N-terminal dual enzyme NatA/Naa50 Complex. Structure 2019;27(7):1057–70. e1054.
[17] Baumgartner JT, et al. Gcn5-related N-acetyltransferases (GNATs) with a catalytic serine residue can play ping-pong too. Front Mol Biosci 2021;8:646046.
[18] Dorfel MJ, Lyon GJ. The biological functions of Naa10 - from amino-terminal acetylation to human disease. Gene 2015;567(2):103–31.
[19] Arnesen T, et al. Proteomics analyses reveal the evolutionary conservation and divergence of N-terminal acetyltransferases from yeast and humans. Proc Natl Acad Sci USA 2009;106(20):8157–62.
[20] Dorfel MJ, Lyon GJ. The biological functions of Naa10 - From amino-terminal acetylation to human disease. Gene 2015;567:103–31.
[21] Lee MN, Kweon HY, Oh GT. N-alpha-acetyltransferase 10 (NAA10) in development: the role of NAA10. Exp Mol Med 2018;50:1–11.
[22] Zhang ZY, Zhang JL, Zhao LX, Yang Y, Guo R, Zhou N, et al. NAA10 promotes proliferation of renal cell carcinoma by upregulating UPK1B. Eur Rev Med Pharm Sci 2020;24:11553–60.
[23] Lim JH, Park JW, Chun YS. Human arrest defective 1 acetylates and activates beta-catenin, promoting lung cancer cell proliferation. Cancer Res 2006;66:10677–82.
[24] Lin YW, Wen YC, Chu CY, Tung MC, Yang YC, Hua KT, et al. Stabilization of ADAM9 by N-alpha-acetyltransferase 10 protein contributes to promoting progression of androgen-independent prostate cancer. Cell Death Dis 2020;11:591.
[25] Yoon H, Kim HL, Chun YS, Shin DH, Lee KH, Shin CS, et al. NAA10 controls osteoblast differentiation and bone formation as a feedback regulator of Runx2. Nat Commun 2014;5:5176.
[26] Zeng Y, Min L, Han Y, Meng L, Liu C, Xie Y, et al. Inhibition of STAT5a by Naa10p contributes to decreased breast cancer metastasis. Carcinogenesis 2014;35:2244–53.
[27] Hua KT, Tan CT, Johansson G, Lee JM, Yang PW, Lu HY, et al. N-alpha-acetyltransferase 10 protein suppresses cancer cell metastasis by binding PIX proteins and inhibiting Cdc42/Rac1 activity. Cancer Cell 2011;19:218–31.
[28] Wang F, Zheng J, Yang J, Luo T, Xu J, Yang Y, et al. N-alpha-Acetyltransferase 10 inhibits invasion and metastasis of oral squamous cell carcinoma via regulating Pirh2-p53 signalling pathway. J Cell Mol Med 2022;26:2921–34.
[29] Seo JH, Park JH, Lee EJ, Vo TT, Choi H, Kim JY, et al. ARD1-mediated Hsp70 acetylation balances stress-induced protein refolding and degradation. Nat Commun 2016;7:12882.
[30] Kang J, Chun YS, Huh J, Park JW. FIH permits NAA10 to catalyze the oxygen-dependent lysyl-acetylation of HIF-1alpha. Redox Biol 2018;19:364–74.
[31] DePaolo JS, Wang Z, Guo J, Zhang G, Qian C, Zhang H, et al. Acetylation of androgen receptor by ARD1 promotes dissociation from HSP90 complex and prostate tumorigenesis. Oncotarget 2016;7:71417–28.
[32] Lee CC, Peng SH, Shen L, Lee CF, Du TH, Kang ML, et al. The Role of N-alphA-acetyltransferase 10 Protein in DNA methylation and genomic imprinting. Mol Cell 2017;68:89–103. e7.
[33] Oladimeji PO, Wright WC, Wu J, Chen T. RNA interference screen identifies NAA10 as a regulator of PXR transcription. Biochem Pharm 2019;160:92–109.
[34] Seo JH, et al. ARD1-mediated Hsp70 acetylation balances stress-induced protein refolding and degradation. Nat Commun 2016;7:12882.
[35] Kuo HP, et al. Phosphorylation of ARD1 by IKKbeta contributes to its destabilization and degradation. Biochem Biophys Res Commun 2009;389(1):156–61.
[36] Wu Y, Lyon GJ. NAA10-related syndrome. Exp Mol Med 2018;50(7):1–10.
[37] Casey JP, Stove SI, McGorrian C, Galvin J, Blenski M, Dunne A, et al. NAA10 mutation causing a novel intellectual disability syndrome with Long QT due to N-terminal acetyltransferase impairment. Sci Rep 2015;5:16022.
[38] Cheng H, Gottlieb L, Marchi E, Kleyner R, Bhardwaj P, Rope AF, et al. Phenotypic and biochemical analysis of an international cohort of individuals with variants in NAA10 and NAA15. Hum Mol Genet 2020;29:877–8.
[39] Lyon GJ, et al. Expanding the phenotypic spectrum of NAA10-related neurodevelopmental syndrome and NAA15-related neurodevelopmental syndrome. Eur J Hum Genet 2023;31(7):824–33.
[40] Esmailpour T, Riazifar H, Liu L, Donkervoort S, Huang VH, Madaan S, et al. A splice donor mutation in NAA10 results in the dysregulation of the retinoic acid signalling pathway and causes Lenz microphthalmia syndrome. J Med Genet 2014;51:185–96.
[41] Forrester S, Kovach MJ, Reynolds NM, Urban R, Kimonis V. Manifestations in four males with and an obligate carrier of the Lenz microphthalmia syndrome. Am J Med Genet 2001;98:92–100.
[42] Bader I, et al. Severe syndromic ID and skewed X-inactivation in a girl with NAA10 dysfunction and a novel heterozygous de novo NAA10 p.(His16Pro) variant - a case report. BMC Med Genet 2020;21(1):153.
[43] McTiernan N, Tranebjaerg L, Bjorheim AS, Hogue JS, Wilson WG, Schmidt B, et al. Biochemical analysis of novel NAA10 variants suggests distinct pathogenic mechanisms involving impaired protein N-terminal acetylation. Hum Genet 2022;141:1355–69.
[44] Saunier C, Stove SI, Popp B, Gerard B, Blenski M, AhMew N, et al. Expanding the phenotype associated with NAA10-related N-terminal acetylation deficiency. Hum Mutat 2016;37:755–64.
[45] Popp B, Stove SI, Endele S, Myklebust LM, Hoyer J, Sticht H, et al. De novo missense mutations in the NAA10 gene cause severe non-syndromic developmental delay in males and females. Eur J Hum Genet 2015;23:602–9.
[46] Salah Ud-Din AI, Tikhomirova A, Roujeinikova A. Structure and functional diversity of GCN5-Related N-Acetyltransferases (GNAT). Int J Mol Sci 2016;17.
[47] Grimsrud PA, et al. A quantitative map of the liver mitochondrial phosphoproteome reveals posttranslational control of ketogenesis. Cell Metab 2012;16(5):672–83.
[48] Lundekvam M, Arnesen T, McTiernan N. Using cell lysates to assess N-terminal acetyltransferase activity and impairment. Methods Enzym 2023;686:29–43.
[49] Aksnes H, Ree R, Arnesen T. Co-translational, Post-translational, and Non-catalytic roles of N-Terminal Acetyltransferases. Mol Cell 2019;73(6):1097–114.
[50] Rope AF, et al. Using VAAST to identify an X-linked disorder resulting in lethality in male infants due to N-terminal acetyltransferase deficiency. Am J Hum Genet 2011;89(1):28–43.
[51] McTiernan N, et al. NAA10 dysfunction with normal NatA-complex activity in a girl with non-syndromic ID and a de novo NAA10 p.(V111G) variant - a case report. BMC Med Genet 2018;19(1):47.
[52] Stenson PD, Ball EV, Mort M, Phillips AD, Shiel JA, Thomas NS, et al. Human Gene Mutation Database (HGMD): 2003 update. Hum Mutat 2003;21:577–81.
[53] Deng S, McTiernan N, Wei X, Arnesen T, Marmorstein R. Molecular basis for N-terminal acetylation by human NatE and its modulation by HYPK. Nat Commun 2020;11:818.
[54] Davis IW, Leaver-Fay A, Chen VB, Block JN, Kapral GJ, Wang X, et al. MolProbity: all-atom contacts and structure validation for proteins and nucleic acids. Nucleic Acids Res 2007;35:W375–83.
[55] Piovesan D, Minervini G, Tosatto SC. The RING 2.0 web server for high quality residue interaction networks. Nucleic Acids Res 2016;44:W367–74.
[56] Schymkowitz J, Borg J, Stricher F, Nys R, Rousseau F, Serrano L. The FoldX web server: an online force field. Nucleic Acids Res 2005;33:W382–8.
[57] Kumar M, Michael S, Alvarado-Valverde J, Meszaros B, Samano-Sanchez H, Zeke A, et al. The Eukaryotic Linear Motif resource: 2022 release. Nucleic Acids Res 2022;50:D497–508.
[58] Pejaver V, Urresti J, Lugo-Martinez J, Pagel KA, Lin GN, Nam HJ, et al. Inferring the molecular and phenotypic impact of amino acid variants with MutPred2. Nat Commun 2020;11:5918.
[59] Kamisetty H, Ovchinnikov S, Baker D. Assessing the utility of coevolution-based residue-residue contact predictions in a sequence- and structure-rich era. Proc Natl Acad Sci USA 2013;110:15674–9.
[60] Sievers F, Wilm A, Dineen D, Gibson TJ, Karplus K, Li W, et al. Fast, scalable generation of high-quality protein multiple sequence alignments using clustal omega. Mol Syst Biol 2011;7:539.
[61] Adzhubei I, Jordan DM, Sunyaev SR. Predicting functional effect of human missense mutations using PolyPhen-2. Curr Protoc Hum Genet Chapter 7: Unit7 20 2013.
[62] Ghosh DK, Pande S, Kumar J, Yesodharan D, Nampoothiri S, Radhakrishnan P, et al. The E262K mutation in Lamin A links nuclear proteostasis imbalance to laminopathy-associated premature aging. Aging Cell 2022;21:e13688.
[63] Ghosh DK, Udupa P, Shrikondawar AN, Bhavani GS, Shah H, Ranjan A, et al. Mutant MESD links cellular stress to type I collagen aggregation in osteogenesis imperfecta type XX. Matrix Biol 2023;115:81–106.
[64] Ghosh DK, Kumar A, Ranjan A. T54R mutation destabilizes the dimer of superoxide dismutase 1(T54R) by inducing steric clashes at the dimer interface. RSC Adv 2020;10:10776–88.
[65] Kumar A, Ghosh DK, Ranjan A. Differential stabilities of mefloquine-bound human and plasmodium falciparum Acyl-CoA-Binding Proteins. ACS Omega 2021;6:1883–93.
[66] Kumar Ghosh D, Nanaji Shrikondawar A, Ranjan A. Local structural unfolding at the edge-strands of beta sheets is the molecular basis for instability and aggregation of G85R and G93A mutants of superoxide dismutase 1. J Biomol Struct Dyn 2020;38:647–59.
[67] Klose DP, Wallace BA, Janes RW. 2Struc: the secondary structure server. Bioinformatics 2010;26:2624–5.
[68] Chen VB, et al. MolProbity: all-atom structure validation for macromolecular crystallography. Acta Crystallogr D Biol Crystallogr 2010;66(Pt 1):12–21.
[69] Emekli U, Schneidman-Duhovny D, Wolfson HJ, Nussinov R, Haliloglu T. HingeProt: automated prediction of hinges in protein structures. Proteins 2008;70:1219–27.
[70] Udupa P, Kumar A, Parit R, Ghosh DK. Acyl-CoA binding protein regulates nutrient-dependent autophagy. Metabolism 2023;145:155338.
[71] Udupa P, Shrikondawar AN, Nayak SS, Shah H, Ranjan A, Girisha KM, et al. Deep intronic mutation in CRTAP results in unstable isoforms of the protein to induce type I collagen aggregation in a lethal type of osteogenesis imperfecta type VII. Biochim Biophys Acta Mol Basis Dis 2023;1869:166741.

[72] Ghosh DK, Roy A, Ranjan A. Aggregation-prOne regions in HYPK help it to form sequestration complex for toxic protein aggregates. J Mol Biol 2018;430(7):963–86.
[73] Ghosh DK, Roy A, Ranjan A. Disordered nanostructure in huntingtin interacting protein K acts as a stabilizing switch to prevent protein aggregation. Biochemistry 2018;57(13):2009–23.
[74] Ghosh DK, Ranjan A. HYPK coordinates degradation of polyneddylated proteins by autophagy. Autophagy 2022;18:1763–84.
[75] Kumar A, Ghosh DK, Ali J, Ranjan A. Characterization of lipid binding properties of plasmodium falciparum acyl-coenzyme a binding proteins and their competitive inhibition by mefloquine. ACS Chem Biol 2019;14:901–15.